

Four-wave resonant interaction of surface gravity waves in finite water depth

S. Liu ^{1,2}, T. Waseda,³ and X. Zhang ^{1,2,*}

¹State Key Laboratory of Ocean Engineering, School of Naval Architecture, Ocean and Civil Engineering, Shanghai Jiao Tong University, Shanghai 200240, China

²Collaborative Innovation Center for Advanced Ship and Deep-Sea Exploration (CISSE), Shanghai 200240, China

³Graduate School of Frontier Sciences, University of Tokyo, Kashiwa, Chiba 277-8563, Japan



(Received 7 July 2022; accepted 24 October 2022; published 22 November 2022)

In this study, we investigated the four-wave resonant and quasis resonant interactions in a special degenerated case, wherein bichromatic mother waves are generated to give birth to a daughter wave. One of the mother waves was counted twice to satisfy the four-wave resonant conditions. Particular attention is paid to the effect of finite water depth. Theoretical analyses based on the Zakharov equation and direct numerical simulations using a higher-order spectral (HOS) method were performed and compared. The present results revealed that both resonant and quasis resonant four-wave interactions were suppressed by the finite depth and eventually attenuated to zero for sufficiently shallow water. It is found that the corresponding critical depth depends on the crossing angle of the initial mother waves. For the two mother waves with a crossing angle $\theta = 25^\circ$, four-wave resonance survives up to $k_1 h \sim 0.57$, where k_1 denotes the wave number of the twice-counted mother wave and h is the water depth. Furthermore, it is found that the four-wave resonant interactions for different values of θ survive up to a global threshold value of $k_1 h \sim 0.4$. In addition, through three-dimensional (3D) Fourier analyses of the results by direct numerical simulations, it is found that the bound wave effects are enhanced, and more harmonics are generated as the water depth decreases.

DOI: [10.1103/PhysRevFluids.7.114803](https://doi.org/10.1103/PhysRevFluids.7.114803)

I. INTRODUCTION

The evolution of random ocean waves is a fundamental and popular research topic, despite being investigated theoretically and experimentally for over 50 years. To describe the evolution of the averaged properties of ocean waves, a statistical theory was established based on the weak nonlinearity and quasi-Gaussian assumptions of a homogeneous wave field, which is often called Hasselmann's equation, or the kinetic equation [1]. Currently, the kinetic equation has been widely adopted in modeling and forecasting the propagation of ocean waves, for example, the third-generation wave models. The basis of kinetic equation is the four-wave resonant interactions.

Four-wave resonant interactions were first described by Phillips [2] and Hasselmann [1] based on the perturbation approach. Let \mathbf{k}_i denote the wave number for different wave components, and ω_i is the corresponding angular frequency. Once the waves fulfill the conditions (i.e., $\mathbf{k}_1 \pm \mathbf{k}_2 \pm \mathbf{k}_3 \pm \mathbf{k}_4 = 0$, $\omega_1 \pm \omega_2 \pm \omega_3 \pm \omega_4 = 0$), resonant interaction occurs, and energy transfer occurs among these different wave components. With considering a special case of $\mathbf{k}_1 = \mathbf{k}_2$, the resonance conditions are reduced to $2\mathbf{k}_1 - \mathbf{k}_3 = \mathbf{k}_4$ with $2\omega_1 - \omega_3 = \omega_4$, which implies that two mother waves 1 and 3 can give birth to a new resonant wave 4. The solutions of this special case correspond to

*xinshuz@sjtu.edu.cn

the well-known figure-of-eight diagram [2]. Based on the perturbation approach, the amplitude of the new resonant wave is expected to increase linearly with the propagation distance [3]. Moreover, Longuet-Higgins [3] showed that the phase angle of the daughter wave is locked to $-\pi/2$ with respect to the mother waves. Experimental validations with respect to the growth rate of daughter wave were performed by Longuet-Higgins and Smith [4], McGoldrick *et al.* [5], and Tomita [6] for perpendicular mother waves. Starting from the quadratic Boussinesq equations, Onorato *et al.* [7] investigated the energy transfer in flat-bottom shallow-water waves, and for the first time found that the four-wave resonant interactions are naturally a part of the shallow water wave dynamics. Recently, to extend the validations of the degenerated resonance theory to more general cases, experiments for oblique mother waves were conducted [8], where theoretical investigation was also performed using Zakharov equation [9]. The experimental results, with the support of theoretical analyses, demonstrated the linear growth of the daughter wave and the phase-locking between resonant waves at small mother-wave steepness. Most of these experimental and theoretical studies were focused on deep water, and it is still unclear whether the non-steady-state four-wave resonance can be depleted by the effect of the finite water depth. Furthermore, to the best of our knowledge, the threshold value, at which the growth rate of the daughter wave diminishes, has not yet been found for four-wave resonance. This is one of the motivations for the present study.

However, the effect of water depth has been studied for modulational instability, which can be considered as a special type of detuned (quasiresonant) four-wave interaction involving collinear waves. In finite depth, wave interaction with the sea bottom generates a wave-induced current that subtracts energy for nonlinear focusing. Consequently, the one-dimensional modulational instability of wave trains to side-band perturbations attenuates and eventually vanishes for sufficiently small water depth, that is, $k_0h < 1.363$, where k_0 denotes the dominant wave number and h denotes the water depth [10,11]. The corresponding theoretical validations were performed for collinear perturbations using Zakharov equation in Janssen and Onorato [12].

When a carrier wave is perturbed by appropriate oblique disturbances, the carrier wave is found to be susceptible to instability even for $k_1h < 1.363$ [13,14]. This result is validated by Toffoli *et al.* [15] based on the experiments and numerical simulations. Furthermore, Fernandez *et al.* [16] found that a carrier wave with oblique perturbations cannot sustain a substantial wave growth for $k_0h < 0.8$. To assess the effects of water depth on modulational instability in realistic wave fields, some attempts have been made for irregular seas. Toffoli *et al.* [17] investigated the effects of directional spreading and finite depth on the statistical properties of surface gravity waves, and the results showed that at intermediate water depths, $k_0h = \mathcal{O}(1)$, the third-order nonlinearity results in weak deviations from Gaussian statistics independent of the degree of directional spreading of wave energy. Fernandez *et al.* [18] assessed the role of modulational instability on wave statistics, particularly on the occurrence of extremes in regular wave fields with different water depths $k_0h = 1.78, 1.30, \text{ and } 1.15$, based on direct numerical simulations. They reported that in relatively shallow water depths, modulational instability has a negligible effect on wave statistics, which are primarily affected by the second-order nonlinearity. It should be remarked that the degenerated case of four-wave resonance focused in the present work is different from the modulational instability. In the degenerated case, it is assumed that $a_4 \ll a_1, a_3$; in the modulational instability we assume $a_3, a_4 \ll a_1$. Thus, the daughter wave grows linearly, but the sideband of modulational waves grows exponentially.

A number of numerical methods solving potential wave equations have been developed to study the resonant wave interactions. For instance, Madsen and Fuhrman [19] presented a new third-order solution for bichromatic bidirectional water waves in finite depth. More recently, Xie *et al.* [20] studied four-wave resonance in deep water using a nonhydrostatic free surface flow model. The effects of wave steepness on the resonant interactions were investigated. They found that strong resonant interactions can lead to the bending and then splitting of crests and troughs. The HOS method proposed by Dommermuth and Yue [21] and West *et al.* [22] has also been widely adopted in the study of the nonlinear wave interactions. Toffoli *et al.* [23] and Xiao *et al.* [24] investigated the evolution of long-crested and short-crested irregular waves through the HOS method. Gramstad

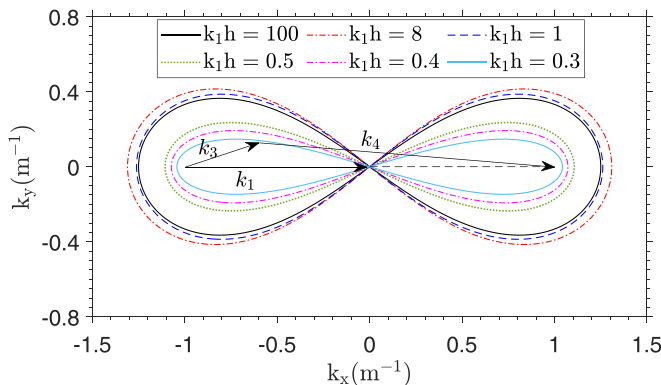


FIG. 1. Solutions of degenerated four-wave resonant conditions ($2\mathbf{k}_1 - \mathbf{k}_3 = \mathbf{k}_4$, $2\omega_1 - \omega_3 = \omega_4$) in different water depths.

et al. [25] simulated the irregular waves with a bi-modal spectral structure. Fedele *et al.* [26] and Fujimoto *et al.* [27] adopted both the third-generation wave model and HOS method to study the occurrence of rogue waves based on field measurements.

The objective of this paper is to investigate the four-wave resonance at finite depth through theoretical analysis based on an analytical model derived from Zakharov equation and direct numerical simulations using the HOS. Both resonant and quasiresonant interactions are studied here. The evolution of the generated daughter-wave amplitude and phase with respect to the mother waves were analyzed. In particular, the effect of water depth was quantified, and further we determined the critical water depth at which the four-wave resonant interaction diminished.

The rest of the paper is organized as follows. Theoretical formulation and analyses are provided in Sec. II. The numerical setup for direct simulation is presented in Sec. III. Results and discussion are described in Sec. IV. The validation of the numerical model is performed firstly by comparison with experimental results from Bonnefoy *et al.* [8] in Sec. IV A. Then, five cases of resonant interactions and five cases of quasiresonant interactions are chosen to study the effect of finite depth on the growth of the daughter wave in Secs. IV B and IV C. The effects of bound and free waves are also investigated. Concluding remarks are given in Sec. V.

II. THEORETICAL FORMULATIONS

A. Resonant interaction theory in finite water depth

Phillips [2] derived for the first time the resonant conditions ($\mathbf{k}_1 + \mathbf{k}_2 = \mathbf{k}_3 + \mathbf{k}_4$, $\omega_1 + \omega_2 = \omega_3 + \omega_4$) with deep-water dispersion relation; the well-known figure-of-eight diagram graphically presented the solutions.

For different water depths, the solutions will be varied because of the dispersion relation. Here, we show how to calculate the resonant conditions of the following degenerate case:

$$2\mathbf{k}_1 - \mathbf{k}_3 = \mathbf{k}_4, \quad (1)$$

and

$$2\omega_1 - \omega_3 = \omega_4, \quad (2)$$

with the linear dispersion relation $\omega^2 = g|\mathbf{k}|\tanh|\mathbf{k}|h$ in finite water depth. Note that for a given mother wave \mathbf{k}_1 , Eqs. (1) and (2) provide three scalar equations for the four scalar components of \mathbf{k}_3 and \mathbf{k}_4 , that is, for k_{3x} , k_{3y} , k_{4x} , and k_{4y} . With the crossing angle θ , the resonant waves \mathbf{k}_3 and \mathbf{k}_4 can be determined. For the sake of simplicity, we assume $\mathbf{k}_1 = (1, 0)$. Figure 1 shows the solutions at different water depths. For each depth, there is a unique resonant curve (that is, the figure-of-eight

diagram). With the crossing angle θ being given, the mother wave \mathbf{k}_3 and daughter wave \mathbf{k}_4 were determined from the curve. As can be seen, the figure-of-eight manifolds tend to enlarge from the deep-water condition up to $k_1 h \sim 3$ and then start to decrease until it becomes similar at $k_1 h \sim 1$ before it becomes smaller beyond that point.

Zakharov equation [9] is one of the main models used to study the evolution of nonlinear surface waves. The interaction kernels $T(\mathbf{k}_1, \mathbf{k}_2, \mathbf{k}_3, \mathbf{k}_4)$ (also written as T_{1234}) and the necessary canonical transformation are described in Krasitskii [28]. The Zakharov equation is derived for an arbitrary constant water depth, but most of its applications are focused on infinite water depth. This may be because the interaction kernel T_{1234} is nonunique for finite water depth, when $\mathbf{k}_3 = \mathbf{k}_1$ and $\mathbf{k}_4 = \mathbf{k}_2$. This nonuniqueness ceases to exist at infinite water depth. To resolve the issue at finite water depth, Janssen and Onorato [12] discussed the special case of T_{1111} . Furthermore, Stiassnie and Gramstad [29] derived the explicit expressions of T_{1212} and the expression for T_{1111} there is identical to the that from Janssen and Onorato [12]. Through these comprehensive expressions from Stiassnie and Gramstad [29], the evolution of bichromatic mother waves which interact with each other at an arbitrary constant water depth can be studied using the Zakharov equation. Four-wave reduced equation for pure gravity wave reads

$$i \frac{\partial \hat{a}_1}{\partial t} = \omega_1 \hat{a}_1 + \int T_{1234} \hat{a}_2^* \hat{a}_3 \hat{a}_4 \delta_{1+2-3-4} d\mathbf{k}_{2,3,4}, \quad (3)$$

where $\hat{a}_i (i = 1, 2, 3, 4)$ are the canonical variables from the complex amplitude A_i through a canonical transformation. By introducing $B_i = \hat{a}_i \exp(i\omega_i t)$, called action amplitude, we obtain

$$i \partial_t B_1 = \int T_{1234} B_2^* B_3 B_4 \delta_{1+2-3-4} \exp(i\Delta_{1234} t) d\mathbf{k}_{2,3,4}, \quad (4)$$

where $\Delta_{1234} = \omega_1 + \omega_2 - \omega_3 - \omega_4$. Because the degenerated four-wave resonance system consists of only three waves including two mother waves 1 and 3, and a daughter wave 4, the discretized evolution equations can be written as follows:

$$i \partial_t B_1 = (\Omega_1 - \omega_1) B_1 + 2T_{1134} \exp(i\Delta_{1134} t) B_1^* B_3 B_4, \quad (5)$$

$$i \partial_t B_3 = (\Omega_3 - \omega_3) B_3 + T_{1134} \exp(-i\Delta_{1134} t) B_1^2 B_4^*, \quad (6)$$

$$i \partial_t B_4 = (\Omega_4 - \omega_4) B_4 + T_{1134} \exp(-i\Delta_{1134} t) B_1^2 B_3^*, \quad (7)$$

where $\Delta_{1134} = 2\omega_1 - \omega_3 - \omega_4$ is the linear detuning factor. $\Omega_i - \omega_i$ is the amplitude dispersion, where Ω_i are the nonlinear frequencies which satisfy the following nonlinear dispersion relations

$$\Omega_1 = \omega_1 + T_{1111} |B_1|^2 + 2T_{1313} |B_3|^2 + 2T_{1414} |B_4|^2, \quad (8)$$

$$\Omega_3 = \omega_3 + 2T_{1313} |B_1|^2 + T_{3333} |B_3|^2 + 2T_{3434} |B_4|^2, \quad (9)$$

$$\Omega_4 = \omega_4 + 2T_{1414} |B_1|^2 + 2T_{3434} |B_3|^2 + T_{4444} |B_4|^2, \quad (10)$$

where the kernel function T can be evaluated based on the formulations given by Janssen and Onorato [12] and Stiassnie and Gramstad [29]. The expressions used for evaluation of the Kernel in the form like T_{1212} is given in Appendix A. To solve Eqs. (5)–(7), it is assumed that the daughter-wave amplitude is small relative to the mother-wave amplitudes, that is, $|B_4| \ll |B_1|, |B_3|$. By applying perturbation analyses on Eqs. (5)–(7), and keeping the terms of B_i up to the first order with respect to ε , the initial stage of evolution of the mother and daughter waves can be written as (the detailed derivation is provided in Appendix B)

$$B_1 = \left\{ B_{10} - 2T_{1134}^2 B_{10}^2 B_{10}^* B_{30}^* B_{30} \left[\frac{1 - \exp(-i\Delta\Omega t)}{\Delta\Omega^2} - \frac{it}{\Delta\Omega} \right] \right\} \exp[i(\omega_1 - \Omega_1)t], \quad (11)$$

$$B_3 = \left\{ B_{30} + T_{1134}^2 B_{10}^2 B_{10}^{*2} B_{30} \left[\frac{1 - \exp(i\Delta\Omega t)}{\Delta\Omega^2} - \frac{it}{\Delta\Omega} \right] \right\} \exp[i(\omega_3 - \Omega_3)t], \quad (12)$$

$$B_4 = -iT_{1134} B_{10}^2 B_{30}^* \frac{\sin(\Delta\Omega t/2)}{\Delta\Omega/2} \exp[-i(\Omega_4 - \omega_4 + \Delta\Omega/2)t] + \text{H.O.T.}, \quad (13)$$

where $\Delta\Omega = 2\Omega_1 - \Omega_3 - \Omega_4$ is the total detuning factor, which includes linear detuning Δ_{1134} and nonlinear detuning. The subscript 0 denotes the initial value. Regarding the derivation of Eq. (13), the reader can refer to Bonnefoy *et al.* [8] and Waseda *et al.* [30]. Here we made an extension of the solutions to the first order in B_4 , and derived new solutions for B_1 and B_3 to account for the effect of the daughter wave on the two mother waves during the initial stage of evolution. By asymptotic analysis of Eqs. (11) and (12), one can show that the magnitude of B_1 decreases whereas B_3 initially increases. This indicates that the energy transfers from mother wave 1 to mother wave 3 and the daughter wave at exact resonance. The comparison of the results using the extended solutions with the direct numerical solutions is shown in Fig. 20 in Appendix B. As shown, the agreement is satisfactory and confirms the findings on the energy exchange between mother waves and the daughter wave. It is worth noting that a formal perturbation analysis will leave extra terms in the evolution equation of B_4 (denoted by H.O.T), but these will not affect the solutions of B_1 and B_3 in the early stage of the resonant interaction.

The relation between free-surface wave amplitude and wave action amplitude is $a_i = \sqrt{2\omega_i/g} B_i$, which is valid for finite water depth. Hence, the amplitude and phase of the daughter wave deduced from Eq. (13) can be written as

$$a_4 = T_{1134} \frac{g}{2\omega_1 k_1^2} \sqrt{\frac{\omega_4}{\omega_3 k_3^2}} \varepsilon_1^2 \varepsilon_3 \left| \frac{\sin(\Delta\Omega t/2)}{\Delta\Omega t/2} \right| t, \quad (14)$$

$$\varphi_4 = -\text{sgn}[\sin(\Delta\Omega t/2)] \frac{\pi}{2} + 2\varphi_{10} - \varphi_{30} - (\Omega_4 - \omega_4 + \Delta\Omega/2)t, \quad (15)$$

where $\varepsilon_i = k_i |a_i|$ is the wave steepness, and the subscript 0 represents the initial value. Using the solutions for B_1 and B_3 , we obtain the mother-wave phases $\varphi_i(t) = -(\Omega_i - \omega_i)t + \varphi_{i0}$ for $i = 1, 3$. With Eq. (15), the interaction phase is introduced as

$$\varphi = 2\varphi_1 - \varphi_3 - \varphi_4 + \frac{\Delta\Omega t}{2} = \text{sgn}[\sin(\Delta\Omega t/2)] \frac{\pi}{2}. \quad (16)$$

It is worth noting that these evolution equations can be transformed from the temporal to the spatial domain based on the relationship $d = c_{g4}t$, where c_{g4} is the group velocity of the daughter wave and d is the distance from the wavemaker measured in the daughter-wave direction. Thus, Eqs. (14) and (16) can be rewritten as

$$a_4 = \varepsilon_1^2 \varepsilon_3 G \left| \frac{\sin(\Delta\Omega d/2c_{g4})}{\Delta\Omega/2c_{g4}} \right| = \varepsilon_1^2 \varepsilon_3 G |\text{sinc}(\Delta\Omega d/2c_{g4})| d, \quad (17)$$

$$\varphi = 2\varphi_1 - \varphi_3 - \varphi_4 + \frac{\Delta\Omega d}{2c_{g4}} = \text{sgn}[\sin(\Delta\Omega d/2c_{g4})] \frac{\pi}{2}, \quad (18)$$

where G is the nondimensional linear growth rate of the daughter-wave amplitude, which is expressed as

$$G = T_{1134} \frac{g}{2\omega_1 k_1^2} \sqrt{\frac{\omega_4}{\omega_3 k_3^2}} \frac{1}{c_{g4}}. \quad (19)$$

It should be noted that Eqs. (17) and (18) together with Eq. (19) are the main derived analytical formulas and the starting point for the following analyses. In the case of infinite depth, these equations can be reduced based on the deep-water dispersion relation, and the resulting expressions are identical to those given in Waseda *et al.* [30] and Bonnefoy *et al.* [8]. However, the analytical

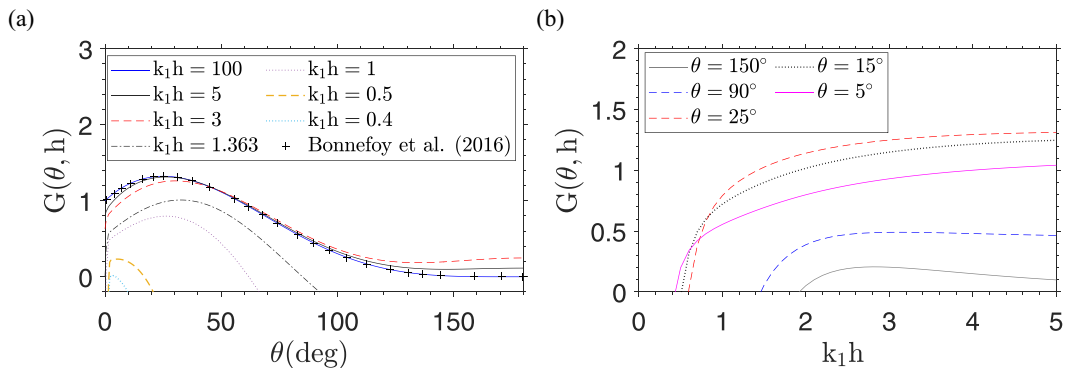


FIG. 2. The resonant growth rate of daughter-wave amplitude obtained from Eq. (19) as a function of (a) crossing angle and (b) nondimensional water depth. The results from Bonnefoy *et al.* [8] for deep-water waves are plotted for comparison.

solutions of Eqs. (17), (18), and (19) can be used to predict the evolution of the daughter wave for an arbitrary water depth such that the effect of the finite water depth can be quantified and analyzed.

B. Theoretical analysis based on analytical formulas

At exact resonance ($\Delta\omega = 0$) and at a short distance ($\Delta\Omega d \ll 1$), now we have $|\sin(\Delta\Omega d/2c_{g4})/(\Delta\Omega/2c_{g4})| \approx d$. Equation (17) predicts linear growth of daughter-wave amplitude and Eq. (18) shows that the interaction phase is locked at $\pi/2$ (equivalent to the fact that the phase of daughter wave is locked at $-\pi/2$ with respect to the mother waves).

For the quasiresonance case [$\Delta\omega \sim O(\varepsilon^2)$], Eq. (17) shows that the daughter-wave amplitude evolves as a $|\sin|$ function with a period of $2\pi c_{g4}/\Delta\Omega$. As can be seen from Eq. (18), the interaction phase is no longer locked at $\pi/2$; instead, it shows a periodic shift between $-\pi/2$ and $\pi/2$ with the same period of $2\pi c_{g4}/\Delta\Omega$ as that for the evolution of amplitude. This is an interesting feature that cannot be observed in infinite water depth [8].

The growth rate depends on the values of the wave numbers $|\mathbf{k}_1|$, $|\mathbf{k}_3|$, $|\mathbf{k}_4|$ and water depth h through the dispersion relation for finite depth. Referring to the solutions of the resonance conditions illustrated in Fig. 1, for a given $|\mathbf{k}_1|$, θ and h , the solutions of $|\mathbf{k}_3|$ and $|\mathbf{k}_4|$ are determined. Thus, assuming $|\mathbf{k}_1| = 1$, the growth rate $G(\theta, h)$ can then be defined as a function of the crossing angle θ and water depth h .

Figure 2(a) illustrates the resonant growth rates as a function of the crossing angle θ and water depth $k_1 h$. The deep-water solutions extracted from Bonnefoy *et al.* [8] (see Fig. 2 therein) were adopted here for reference. As shown in Fig. 2(a), the present results at $k_1 h = 100$ are in good agreement with Bonnefoy *et al.* [8]. The growth rate G at $\theta = 0^\circ$ for $k_1 h \leq 1.363$ is found to be zero. This is because the interaction kernel T_{1134} reduces to T_{1111} in the collinear case and diminishes to zero as $k_1 h \leq 1.363$ [12], which is the critical depth for modulational instability in the collinear case. In addition, the curve of G at $k_1 h = 0.4$ suggests that almost all the four-wave resonances with different crossing angles cannot survive as $k_1 h < 0.4$.

As shown in Fig. 2(b), for a given crossing angle of less than 90° , i.e., $\theta = 5^\circ$, 15° , or 25° , the growth rate of daughter-wave amplitude is suppressed by decreasing water depth from $k_1 h = 100$. As the depth becomes sufficiently shallow, the growth rate eventually approaches zero. For a large crossing angle, we find that the growth rate increases first and reaches a maximum at approximately $k_1 h \sim 3$, and then decreases as the water depth becomes shallower. For instance, as shown in Fig. 2(b), for crossing angle $\theta = 150^\circ$, the growth rate gradually increases as the water depth decreases from $k_1 h = 5$ to $k_1 h = 3$, and then reaches a maximum around $k_1 h \sim 2.8$ before it decreases to zero as the water depth further reduces. Another interesting feature, as can be observed,

is that the corresponding critical depth at which the growth rate diminishes depends on the crossing angle θ . As the crossing angle approaches zero, the critical depth reduces continuously. The critical depth is $k_1 h = 0.57$ for $\theta = 25^\circ$.

III. SETUP FOR DIRECT NUMERICAL SIMULATION

Assuming an irrotational, inviscid, and incompressible flow with constant water depth, the velocity potential $\phi(x, y, z, t)$ in the fluid domain satisfies the Laplace equation. On the free surface $z = \eta(x, y, t)$, the kinematic and dynamic boundary conditions in the Zakharov's form are written as

$$\eta_t = -\nabla\eta \cdot \nabla\phi^s + (1 + |\nabla\eta|^2) \cdot \phi_z, \quad (20)$$

$$\phi_t^s + g\eta = -\frac{1}{2} \cdot |\nabla\phi^s|^2 + \frac{1}{2}(1 + |\nabla\eta|^2)\phi_z^2, \quad (21)$$

where $\phi^s(\mathbf{x}, t) = \phi(\mathbf{x}, \eta(\mathbf{x}, t), t)$ is the surface velocity potential, $\eta(\mathbf{x}, t)$ is the surface elevation, $\mathbf{x} = (x, y)$ and $\nabla = (\partial/\partial x, \partial/\partial y)$.

At the sea bottom ($z = -h$), the boundary condition is

$$\phi_z = 0. \quad (22)$$

To investigate the evolution of the resonant wave system, we directly solved the field equation with boundary conditions using a HOS method proposed by Dommermuth and Yue [21] and West *et al.* [22]. This is a pseudospectral method that uses a series expansion in terms of the wave steepness of the velocity potential and the vertical velocity on the free surface. Here, we considered a third-order expansion (order of nonlinearity $M = 3$) so that both three- and four-wave interactions are included [31,32]. Moreover, we adopted higher-order expansion (up to $M = 5$) to examine the effect of higher-order nonlinearity. Our results showed the growth rates of the daughter wave using $M = 3$ and $M = 5$ were almost the same. The HOS has been widely adopted in the modeling of the gravity waves (e.g., [23,24,33]). We have developed our own version of the HOS code using the GPU-accelerated computing technique. It is important to mention that the present model does not include effects related to the bottom topography (i.e., a flat-bottom boundary condition is assumed here). Although the HOS method has been adopted by many researchers (e.g., [31,32]) to study the nonlinear evolution of a random wave field, a precise validation to reproduce the four-wave resonant interaction has never been performed before.

The HOS method requires appropriate initial conditions for the surface elevation and the corresponding velocity potential. In this study, the initial two mother waves are generated first to give birth to a new resonant wave (also called a daughter wave). The input parameters include the mother-wave wave numbers (\mathbf{k}_1 and \mathbf{k}_3), wave steepness (ε_1 and ε_3), propagation directions (θ_1 and θ_3), and the water depth h . For simplicity, the propagation direction for mother wave 1 is fixed as $\theta_1 = 0^\circ$.

Three sets of simulations were carried out: Sets A and B for resonant interactions and Set C for quasiresonant cases. In the first set of simulations (Set A), we studied the resonant interactions in deep water and compared the solutions with the experiments in Bonnefoy *et al.* [8]. The wave numbers $|\mathbf{k}_1|$ and $|\mathbf{k}_3|$ employed here are: $|\mathbf{k}_1| = 3.28$, $|\mathbf{k}_3| = 2.06$. The crossing angle was fixed at $\theta = 25^\circ$ to achieve a significant growth of the daughter wave, as suggested in Fig. 2(a). The wave steepness for one of the mother waves varies from low to higher values: fixed $\varepsilon_3 = 0.05$ and varied $\varepsilon_1 = 0.028, 0.041, 0.056$. To study the effects of water depth, resonant interactions at five different depths $h = 1.15, 0.75, 0.45, 0.30$, and 0.15 m (corresponding to $k_1 h = 3.65, 2.24, 1.35, 0.95$, and 0.57 , respectively) are simulated in Set B. As the resonant conditions are modified with the change in the dispersion relation, the value of wave number $|\mathbf{k}_1|$ is varied while $|\mathbf{k}_3| = 2.06$ and $\theta = 25^\circ$ are fixed to fulfill the exact resonance conditions at different water depths (see Fig. 1).

TABLE I. Key parameters in the cases chosen for direct numerical simulations of the resonant and quasiresonant wave systems using the HOS method. We consider cases (Set A and Set B) when $\Delta\omega < 0.005$ as “exact” resonance. Set B is configured for exact resonance case in finite water depth. Set C is the quasiresonant case in finite water depth.

	$k_1(\text{m}^{-1})$	$k_3(\text{m}^{-1})$	$k_4(\text{m}^{-1})$	ε_1	ε_3	$\theta(\text{deg})$	$h(\text{m})$	$k_1 h$	$\Delta\omega(\text{rad/s})$
Set A	3.270	2.062	4.753	0.028	0.050	25	100	327	0.0026
	—	—	—	0.041	—	—	—	—	—
	—	—	—	0.056	—	—	—	—	—
Set B	3.177	2.062	4.569	0.056	0.050	25	1.15	3.65	0.0045
	2.990	—	4.203	—	—	—	0.75	2.24	0.0033
	2.990	—	4.203	—	—	—	0.45	1.35	0.0026
	3.177	—	4.203	—	—	—	0.30	0.95	0.0002
	3.831	—	5.859	—	—	—	0.15	0.57	-0.0005
Set C	3.270	2.062	4.753	0.056	0.050	25	1.15	3.76	0.0400
	—	—	—	—	—	—	0.75	2.45	0.1241
	—	—	—	—	—	—	0.45	1.47	0.1706
	—	—	—	—	—	—	0.30	0.98	0.0646
	—	—	—	—	—	—	0.15	0.49	-0.1678

In addition, we investigated the four-wave quasiresonant interactions in Set C. The wave numbers of the mother waves \mathbf{k}_1 and \mathbf{k}_3 are chosen to be the same as those defined in Set A. These deep-water resonant waves cannot trigger exact resonance at a finite water depth; however, quasiresonant or near-resonant interactions can be induced. Five different water depths $h = 1.15, 0.75, 0.45, 0.30, 0.15$ m (corresponding to $k_1 h = 3.76, 2.45, 1.47, 0.98, 0.49$, respectively) are considered. The key parameters of the mother and daughter waves with the corresponding detuning factors are summarized in Table I. The detuning factor is calculated as $\Delta\omega = 2\omega_1 - \omega_3 - \omega_4$, where ω_i is the linear frequency. It is worth noting that the HOS method cannot simulate exact resonance (i.e., $\Delta\omega = 0$) owing to the bounded wave number resolution. However, we try to minimize the mismatch of the frequency. Herein, we define the “exact” resonance condition the detuning factor is small enough such that $\Delta\omega < 0.005$.

The computational domain is a rectangle of $20\lambda_{3x} \times 10\lambda_{3y}$, where λ_{3x} and λ_{3y} are the wavelengths corresponding to components of the wave number \mathbf{k}_3 in the x and y directions, respectively. It should be noted that the resolution in wave number domain is determined by the dimensions of the computational domain in x direction L_x and y direction L_y : $\Delta k_x = 2\pi/L_x$ and $\Delta k_y = 2\pi/L_y$. The computational domain ensures that \mathbf{k}_3 is precisely captured in the present numerical model, whereas \mathbf{k}_1 may be slightly off from the desired wave number satisfying the exact resonance conditions. Consequently, exact resonant interactions can hardly be formed in the HOS simulations, but we keep $\Delta\Omega$ as small as possible. The detuning factor values for each case are listed in Table I. A total of 512×256 nodes is selected to capture the surface elevation and velocity potential. The fourth-order Runge-Kutta time-stepping scheme with $\Delta t = T_4/32$ is adopted, where T_4 is the period of the daughter wave. The simulation duration was set as $t = 128T_4$. An adjustment scheme for approximately $10T_4$ was applied here for the initialization of nonlinear waves [34]. In the following figures, the ending time of the adjustment scheme $t = 10T_4$ is shifted to zero for convenience.

The space-time data of free-surface elevation from HOS simulations allow us to study the evolution of daughter waves and validate the theoretical results by the Zakharov equation. Usually, a two-dimensional Fourier transform $\hat{F}\{\eta(x, y)\}$ is applied to the surface elevation at each time step to calculate the daughter-wave amplitude and the phase angle. However, the amplitude and phase of the bound waves are also included at the same wave number as the free-wave component. To quantify the effect of the bound wave, a three-dimensional fast Fourier transform (3D-FFT) of the space-time data $\hat{F}\{\eta(x, y, t)\}$ is adopted. With this approach, the space-time spectrum is fully captured, and

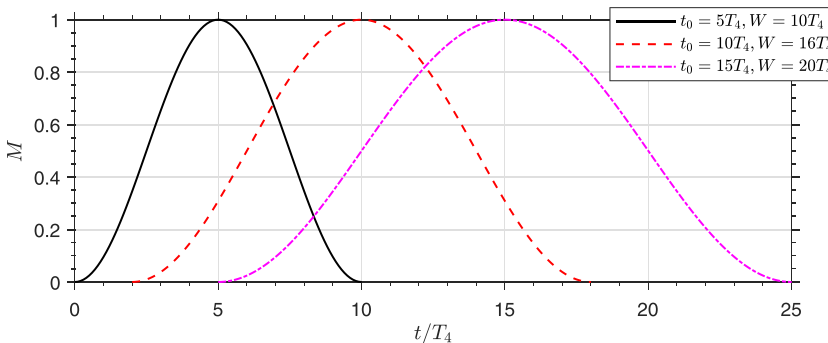


FIG. 3. Examples of the window function for the three-dimensional Fourier transform.

hence the free waves and bound waves can be easily distinguished through the linear dispersion relation curve. This three-dimensional Fourier transform of the surface elevations is performed with a window function of time $M(t)$ defined as follows [35]:

$$M(t) = \frac{1}{2} - \frac{1}{2} \cos \frac{2\pi(t - t_0 + W/2)}{W}, \quad t_0 - W/2 \leq t \leq t_0 + W/2, \quad (23)$$

where W is the duration of time of the window function. t_0 is the central time point. Examples of the window function with different values of W and t_0 are shown in Fig. 3. This window function selects the time slice of length W centered at t_0 and smoothly damps the data at the window edges, which allows us to analyze the space-time spectra for different times. The frequency resolution of 3D-FFT is inversely proportional to the length W . Thus, the selected W should ensure enough frequency resolution and not include too many times. Here, we used $W = 10T_4$ and $t_0 = 5T_4, 10T_4, \dots, 100T_4$ to calculate the space-time spectra at different times.

IV. RESULTS AND DISCUSSION

A. Resonant four-wave interaction in deep water

First, we study the resonant interactions between gravity waves in deep water. To examine the evolution of the surface elevation and localized wave shape in the wave field, typical examples recorded at $t/T_4 = 0, 64, \text{ and } 128$ are presented in Fig. 4. Figures 4(a)–4(c) show the top views of the wave shape in a field of $20 \text{ m} \times 20 \text{ m}$. The dotted black lines represent crest lines of surface elevation which are perpendicular to the propagating directions of the included wave components in the wave field. As shown in the Fig. 4(a), the crest lines were found to be along with the directions around 90° and 65° . The two crest lines confirm that the initial wave field consists of two different wave components \mathbf{k}_1 and \mathbf{k}_3 , propagating in 0° and 25° , respectively. As the waves evolve, a new crest line along 79° is observed, which indicates a new wave component propagating in the direction of around 11° . This is a direct signature for the generation of a daughter wave by resonant interactions. Furthermore, it is observed that, as the wave evolves, the individual crest tends to be slightly rotated clockwise and divided into two parts, which can explain the emergence of the new crest line. The detailed formation process of the oblique localized crest is illustrated in Figs. 4(d)–4(f). As can be observed, the individual crest is divided into an “old” crest accompanied by a relatively smaller “new” crest. A similar phenomenon was observed in the numerical simulation of narrow-banded wave groups [36]. In addition, we have confirmed that this “new” crest phenomenon and wave shape do not depend on the initial phases of the mother waves, which is consistent with the phase-locking mechanism formulated in Eq. (18).

Figure 5 shows the spatial amplitude spectra at different times, including the simplified directional spectra [Figs. 5(a)–5(c)] and omnidirectional spectra [Figs. 5(d)–5(f)]. The peak emerging at

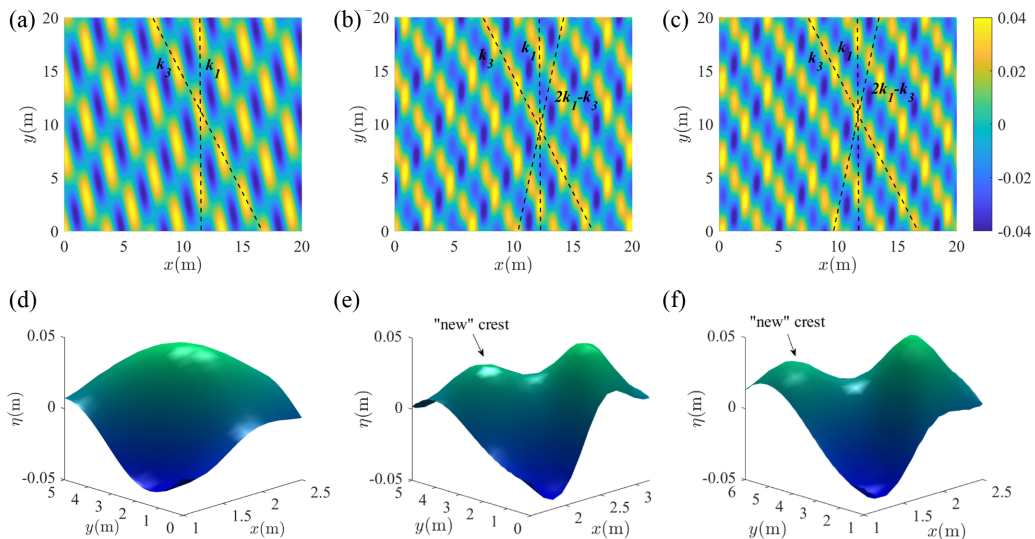


FIG. 4. Free-surface elevation (a–c) and corresponding localized crest shape (d–f) in deep-water resonant case (Set A, $\varepsilon_1 = 0.056$) measured at different times: $t/T_4 = 0$ (a, d), 64 (b, e), and 128 (c, f).

wave number $|2\mathbf{k}_1 - \mathbf{k}_3|$ both in the directional and unidirectional spectrum is direct evidence of the generation of the daughter wave because of resonant interactions. From Figs. 5(d)–5(f), it can be observed that the amplitude of mother wave 1 decreases gradually while that of mother wave 3 increases slightly, which is consistent with the analyses performed using Eqs. (11) and (12) (see Appendix B).

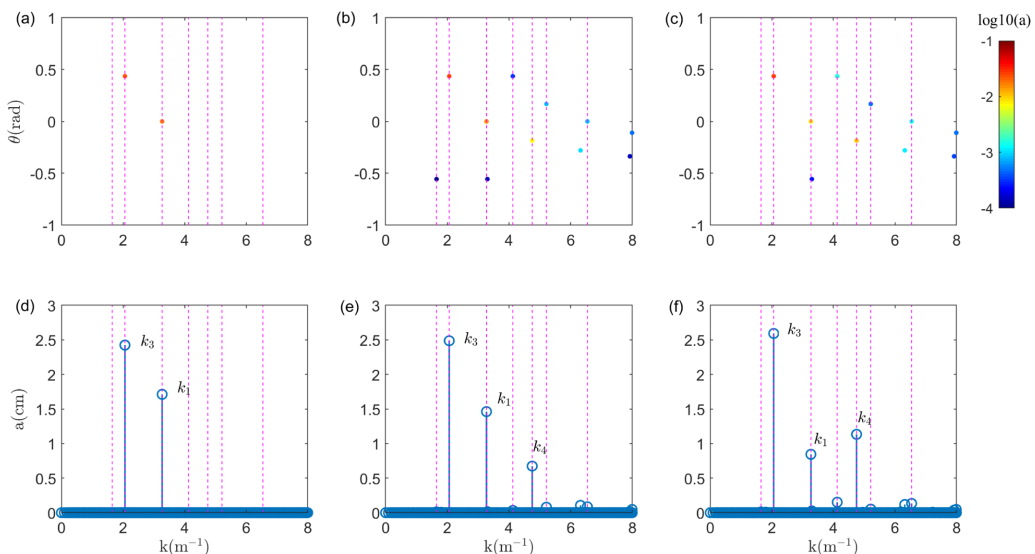


FIG. 5. Directional spectra (a–c) and unidirectional spectra (d–f) in deep-water resonant case (Set A, $\varepsilon_1 = 0.056$). Different columns correspond to the spectra recorded at different times: $t/T_4 = 0$ (a, d), 64 (b, e), and 128 (c, f). Vertical dotted lines denote the wave numbers in order of: $|\mathbf{k}_1 - \mathbf{k}_3|$, $|\mathbf{k}_3|$, $|\mathbf{k}_1|$, $|2\mathbf{k}_3|$, $|2\mathbf{k}_1 - \mathbf{k}_3|$, $|\mathbf{k}_1 + \mathbf{k}_3|$, and $|2\mathbf{k}_1|$.

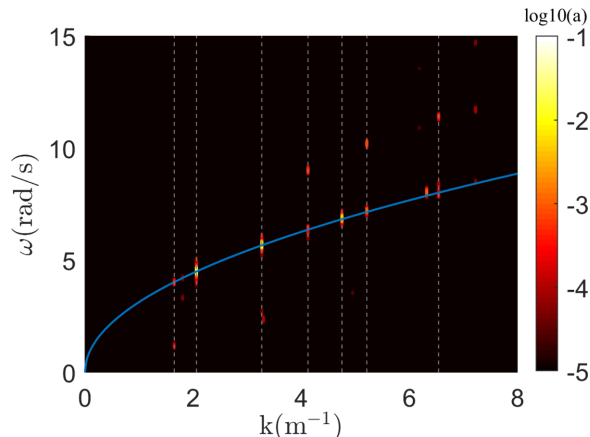


FIG. 6. The space-time spectrum in deep-water resonant case (Set A, $\varepsilon_1 = 0.056$). The solid line represents the linear dispersion relation. Vertical dashed lines denote the components at wave numbers in order of: $|\mathbf{k}_1 - \mathbf{k}_3|$, $|\mathbf{k}_3|$, $|\mathbf{k}_1|$, $|2\mathbf{k}_3|$, $|2\mathbf{k}_1 - \mathbf{k}_3|$, $|\mathbf{k}_1 + \mathbf{k}_3|$, $|2\mathbf{k}_1|$. A time-window function $M(t)$ with $W = 64T_4$, $t_0 = 50T_4$ is used to obtain this spectrum.

We also noticed that the emergence of peaks at wave numbers $|2\mathbf{k}_3|$, $|2\mathbf{k}_1|$, $|\mathbf{k}_1 + \mathbf{k}_3|$ and $|\mathbf{k}_1 - \mathbf{k}_3|$, although the amplitudes are much smaller than those of the daughter wave. These are likely the signatures of second-order nonlinear effects, but the peaks may include contributions from both the bound and free waves.

To distinguish between bound and free waves, the space-time amplitude spectrum $S(k, \omega)$ was analyzed using 3D-FFT, as shown in Fig. 6. A time-window function (23) with $W = 32T_4$, $t_0 = 50T_4$ is applied. The solid blue line in the k - ω plot represents the linear dispersion relation and allows us to distinguish the free and bound wave components, respectively. Higher-order harmonics at $|2\mathbf{k}_3|$, $|2\mathbf{k}_1|$, $|\mathbf{k}_1 + \mathbf{k}_3|$ and $|\mathbf{k}_1 - \mathbf{k}_3|$ in Fig. 5 represent the total energy of both free waves, that lie on the blue line in Fig. 6, and bound waves that do not. What is peculiar is the emergence of free waves at $|\mathbf{k}_1 + \mathbf{k}_3|$ and $|\mathbf{k}_1 - \mathbf{k}_3|$, whose amplitudes are much smaller than the daughter-wave at $|2\mathbf{k}_1 - \mathbf{k}_3|$. Furthermore, only the free wave is found at $|2\mathbf{k}_1 - \mathbf{k}_3|$ and the bound wave effect on the daughter wave is negligible.

For a quantitative comparison with the experimental observations, the evolution of the daughter-wave amplitude in the initial stage is presented in Fig. 7(a). The theoretical predictions for different wave steepness are plotted in solid lines. It should be noted that our numerical results were converted from the temporal domain to the spatial domain using the group velocity c_{g4} . At short distances, the daughter-wave amplitude was found to be in quantitative agreement with both the experimental and theoretical results. However, with the growth of the daughter wave, the entire wave systems do not satisfy the small-amplitude assumption adopted in resonant wave interaction theory; thus, the discrepancy between theoretical solutions and the present results by the HOS method becomes more noticeable, in particular in cases with large wave steepness. The HOS results indicate that the growth rate tends to be attenuated after a longer time, which is more substantial as the mother-wave steepness ε_1 increases. Figure 7(b) illustrates the evolution of the sine of the interaction phase angle $\varphi = 2\varphi_1 - \varphi_3 - \varphi_4$ from HOS simulations. As shown, during the initial stage, the interaction ($d \ll 2$ m) phase increases rapidly to $\pi/2$ and then remains unvaried for long distances, particularly for small mother-wave steepness (e.g., $\varepsilon_1 = 0.028$). This phase-locking phenomenon agrees well with the theoretical predictions from Eq. (15) and the experimental observations of Bonnefoy *et al.* [8]. For large wave steepness, we find there is a gradual reduction in $\sin \varphi$.

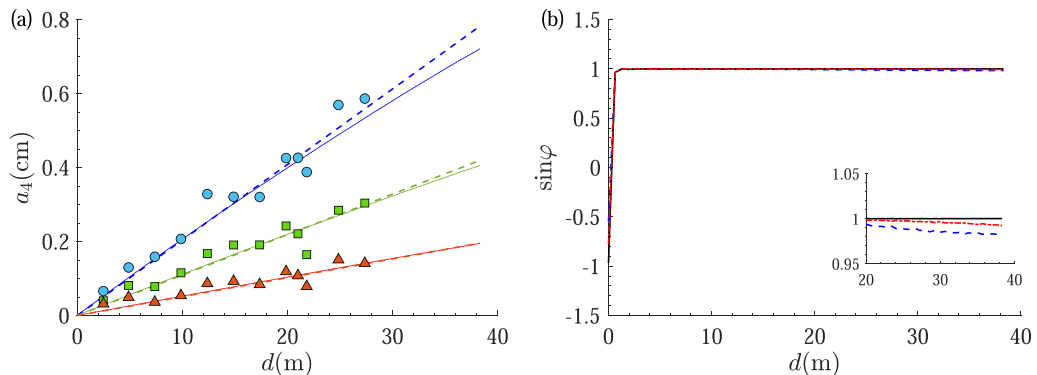


FIG. 7. Evolution of deep-water resonant waves (Set A). (a) Development of daughter-wave amplitude a_4 with fixed $\epsilon_3 = 0.05$ and different $\epsilon_1 = 0.028, 0.041, 0.056$ (from bottom to top: red, green, and blue lines, respectively). The solid lines represent the HOS results. The experimental results in Bonnefoy *et al.* [8] are plotted in markers. Theoretical results using Eq. (14) are plotted in dashed lines. (b) The evolution of the sine of the interaction phase $\varphi = 2\varphi_1 - \varphi_3 - \varphi_4$ from HOS simulations, $\epsilon_1 = 0.028$ (—), 0.041 (- · -), 0.056 (---).

B. Resonant four-wave interaction in finite depth

Herein we investigate the effect of water depth on the resonant interactions by applying the same kind of analysis performed in Sec. IV A to the results of Set B, as listed in Table I, using HOS simulations. Figure 8 shows the simplified directional spectra (a–c) and unidirectional spectra (d–f) for a finite water depth $k_1 h = 0.95$. Again, the peak observed at wave number $|2\mathbf{k}_1 - \mathbf{k}_3|$ confirms the existence of the daughter wave. The overall structure of the spectrum is similar to that of the deep water case (Fig. 5); however, a slight difference is found in the relative magnitudes of

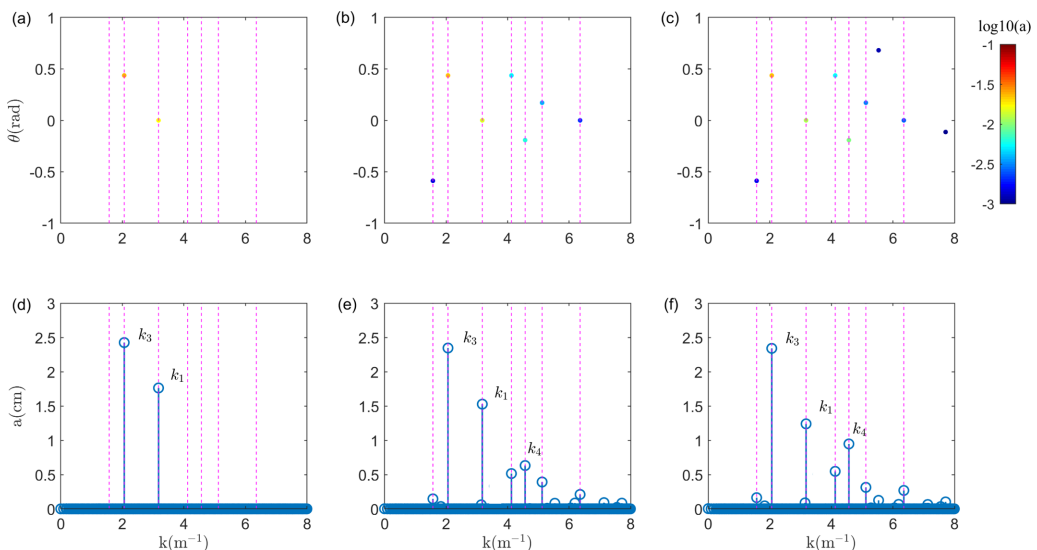


FIG. 8. Directional spectra (a–c) and unidirectional spectra (d–f) in finite-depth resonant cases (Set B) recorded at different times: $t/T_4 = 0$ (a, d), 64 (b, e), and 128 (c, f). Vertical dotted lines denote the wave numbers in order of: $|\mathbf{k}_1 - \mathbf{k}_3|$, $|\mathbf{k}_3|$, $|\mathbf{k}_1|$, $|2\mathbf{k}_3|$, $|2\mathbf{k}_1 - \mathbf{k}_3|$, $|\mathbf{k}_1 + \mathbf{k}_3|$, and $|2\mathbf{k}_1|$. Conditions: $\epsilon_1 = 0.056$, $\epsilon_3 = 0.050$, and $k_1 h = 0.95$.

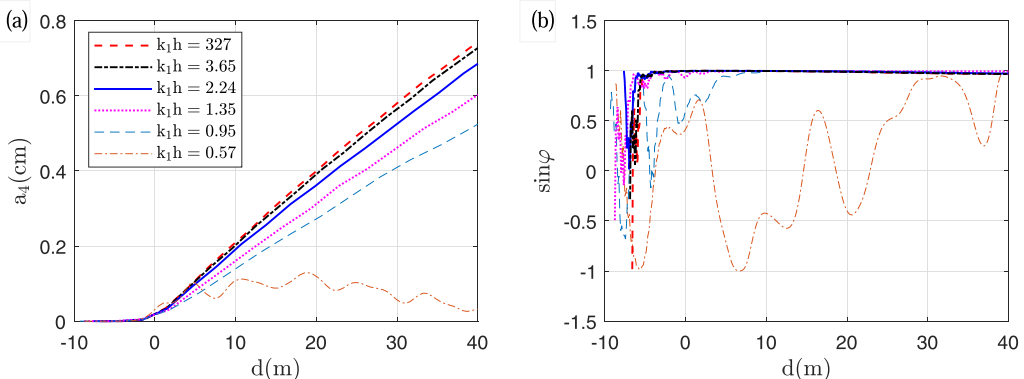


FIG. 9. Evolution of resonant waves in finite water depth (Set B): (a) daughter-wave amplitude; (b) the sine of interaction phase.

the daughter wave and the mother waves. In addition, the magnitudes of the waves at the bound frequency components appear to be larger than those in the deep-water case.

To quantify and examine the effect of water depth, the daughter-wave amplitude and interaction phase for different water depths were computed and illustrated in Fig. 9. The ending time of the nonlinear adjustment scheme [34] $t = 10T_4$ is shifted to $t = 0$. We found that the growth rate is gradually reducing with the decrease of water depth to $k_1h < 1.35$ for crossing angle $\theta = 25^\circ$. In much shallower depth $k_1h = 0.95$, the linear growth of daughter-wave amplitude and phase-locking phenomenon still exist. However, it is interesting to see that, when the water depth gets shallow enough to $k_1h = 0.57$, the linear growth of the daughter wave disappears. Further, as shown by the solid black lines for $k_1h = 0.57$, the amplitude of the daughter wave for large d is much smaller than the other cases and the interaction phase changes irregularly, which implies the energy transfer between mother waves and daughter wave is negligible. This further suggests that the degenerated four-wave resonant interaction ceases to exist at $k_1h = 0.57$ for $\theta = 25^\circ$, which agrees with the prediction by the theoretical model based on the Zakharov equation, as illustrated in Fig. 2(b). It should be noted that, in the present HOS simulations the mother waves \mathbf{k}_1 and \mathbf{k}_3 are precisely captured, correspondingly the daughter wave $2\mathbf{k}_1 - \mathbf{k}_3$ is also precisely captured. The disappearance of the linear growth of the daughter wave cannot be attributed to discreteness of the computational domain.

A three-dimensional fast Fourier transform of spatial-temporal data $\eta(x, y, t)$ is conducted to evaluate the effect of bound waves on daughter-wave development at finite water depth. As an example, the k - ω spectra at $t = 50T_4$ for different depths are illustrated in Fig. 10. As shown in the different panels of the figure, as the water depth decreases from $k_1h = 3.65$ to $k_1h = 1.35$, the two components $|2\mathbf{k}_3|$ and $|2\mathbf{k}_1 - \mathbf{k}_3|$, denoted by the white dashed vertical lines, get close to each other, which is consistent with the variation in the figure-of-eight diagrams with the finite water depth, as illustrated in Fig. 1. In addition, we can observe that for relatively higher depths $k_1h = 3.65, 2.24$, and 1.35 the wave energy at $|2\mathbf{k}_1 - \mathbf{k}_3|$ is concentrated on the linear dispersion curve, and thus includes only the free-wave component and not the bound-wave component. For shallower depths, $k_1h = 0.95$ and 0.57 , the energy is distributed between the free wave on the linear dispersion curve and the bound-wave components at higher angular frequencies. Besides, it is found that the effect of bound wave becomes more pronounced as the water depth decreases, which is consistent with the finding in Toffoli *et al.* [37].

To eliminate the effect of bound waves on the growth of daughter waves, the space-time spectra for these two cases ($k_1h = 0.95$ and 0.57) were evaluated every five periods using the three-dimensional fast Fourier transform (3D-FFT) with a time-window length $W = 10T_4$. The evolution of the free-wave amplitude and phase were obtained (Fig. 11) and compared with the

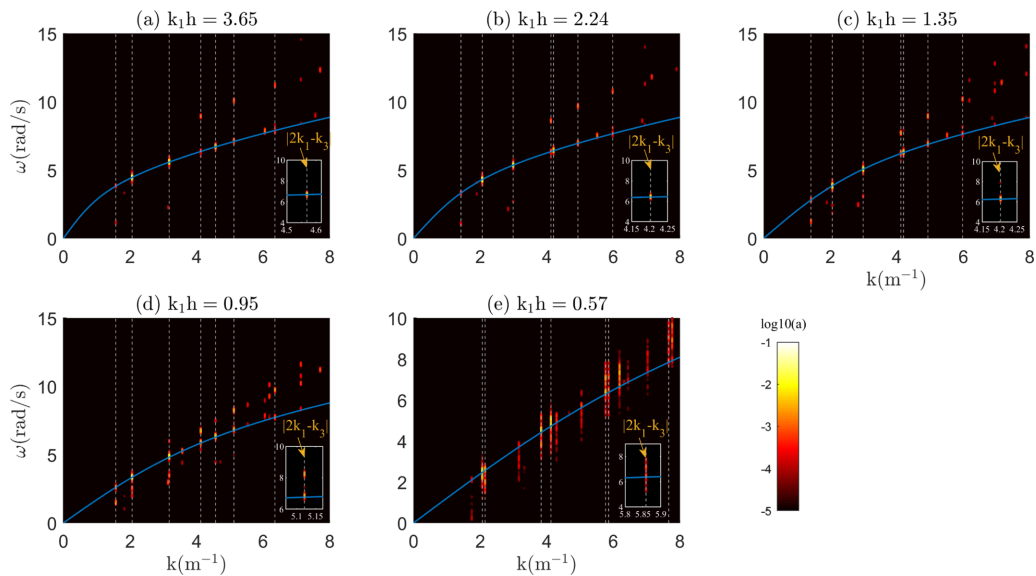


FIG. 10. Space-time spectra in finite-depth resonant cases (Set B). The solid line represents the linear dispersion relation. Vertical dotted lines denote the wave numbers in the order of: $|\mathbf{k}_1 - \mathbf{k}_3|$, $|\mathbf{k}_3|$, $|\mathbf{k}_1|$, $|2\mathbf{k}_3|$, $|2\mathbf{k}_1 - \mathbf{k}_3|$, $|\mathbf{k}_1 + \mathbf{k}_3|$, and $|2\mathbf{k}_1|$. The region around $|2\mathbf{k}_1 - \mathbf{k}_3|$ is magnified in the subplot of each panel. The time-window function $M(t)$ with $W = 32T_4$, $t_0 = 50T_4$ is used to obtain these spectra.

results that included both free and bound waves (Fig. 9). With bound waves, the daughter-wave amplitude increases slightly for $k_1h = 0.95$, while the interaction phase changes slightly. However, as the water depth decreases to $k_1h = 0.57$, the bound wave effect becomes substantial. At this water depth, the free-wave amplitude is approximately not varied with time, which indicates that this is a spurious free wave.

To validate the separation method for the free and bound harmonics based on a windowed 3D-FFT, the bound wave amplitudes at $|2\mathbf{k}_1|$, $|2\mathbf{k}_3|$, $|\mathbf{k}_1 + \mathbf{k}_3|$, and $|\mathbf{k}_1 - \mathbf{k}_3|$ are compared with the second-order theoretical results from Toffoli *et al.* [37], Dalzell [38] in Fig. 12. The red dots correspond to the HOS results using a windowed 3D-FFT. The blue lines represent the second-order

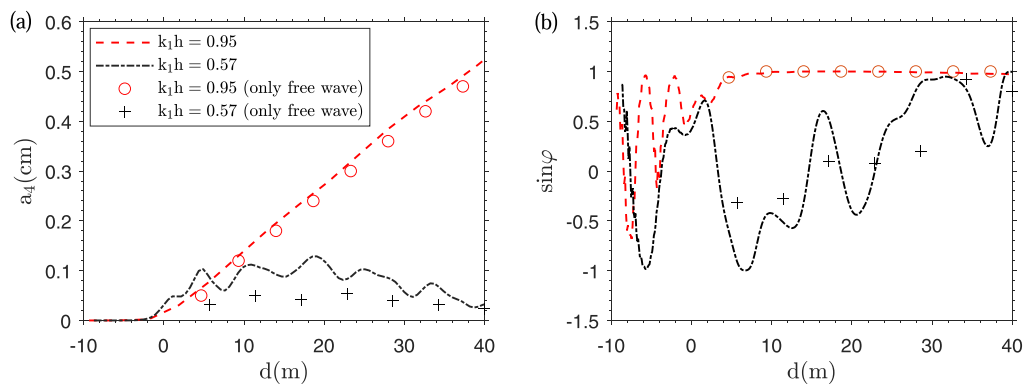


FIG. 11. Effect of bound waves on the evolution of the daughter wave in resonant interactions of Set B: (a) wave amplitude, (b) interaction phase.

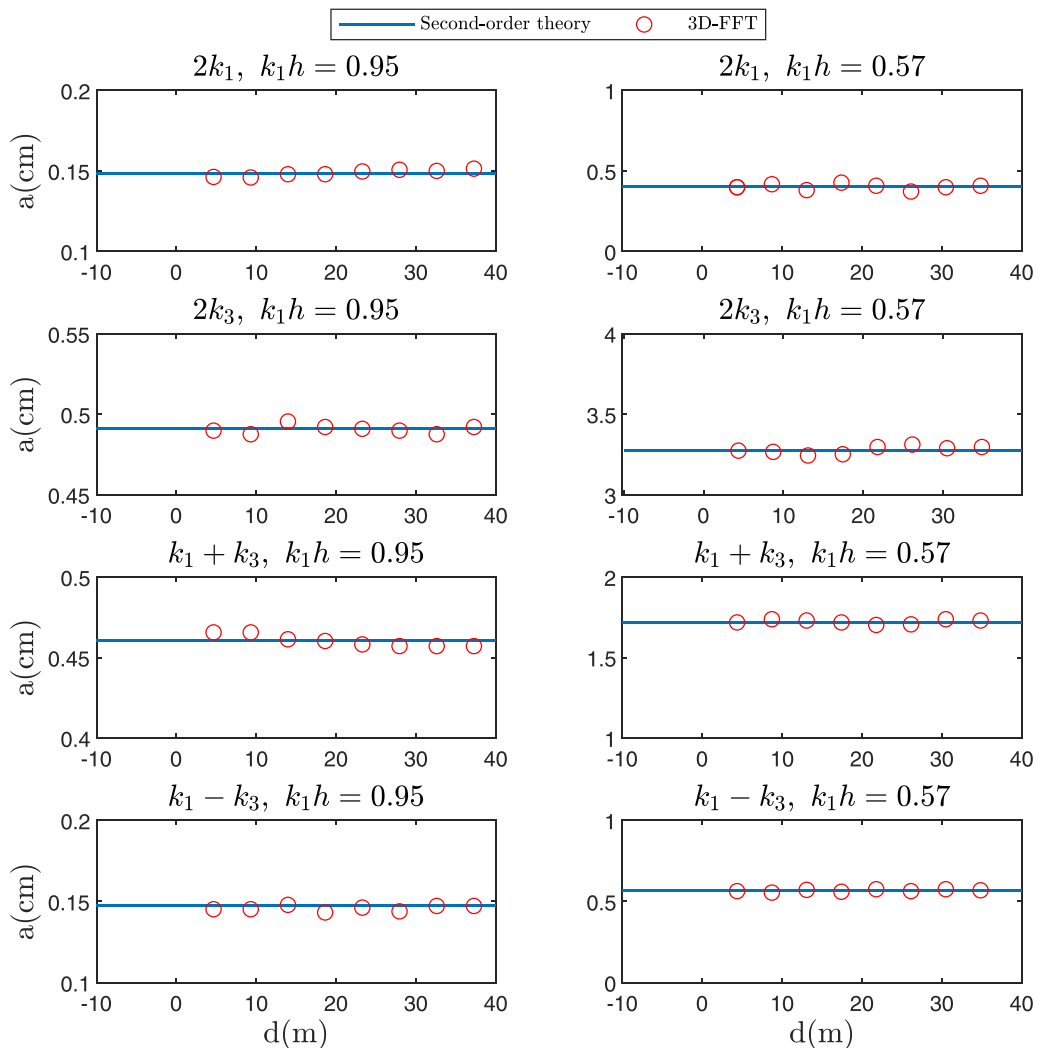


FIG. 12. Evolution of bound-wave components at $|2\mathbf{k}_1|$, $|2\mathbf{k}_3|$, $|\mathbf{k}_1 + \mathbf{k}_3|$, $|\mathbf{k}_1 - \mathbf{k}_3|$. The solid lines denote the second-order theoretical predictions. The red circles represent the results from HOS simulations using the 3D-FFT.

predictions. A satisfactory agreement is found which provides a robust validation of the separation of the free and bound waves.

To quantitatively compare the results of HOS and the analytical solutions using the Zakharov equation, the first step is to calculate the growth rate of a_4 during the initial stage from Fig. 9. Herein, we used linear fitting $a_4 = \tilde{G}d$ by the least-squares method in the initial stage of evolution, around $0 \sim 30$ m. It can be found that the amplitude of the daughter wave is still much smaller than the mother waves at $d = 30$ m (see Fig. 20 in Appendix B). The second step is to compute the re-scaled growth rate G through the relationship $G = \tilde{G}/\varepsilon_1^2\varepsilon_3$. The present analytical solutions of Eq. (19) involves only the interaction of free waves, whereas HOS simulations include both bound and free waves. The space-time spectrum analysis allows us to distinguish them (see Fig. 11). The results with and without bound waves are compared in Fig. 13. As shown, at relatively large water depth, the effect of the bound wave is minimal, and the HOS results are in satisfactory agreement with

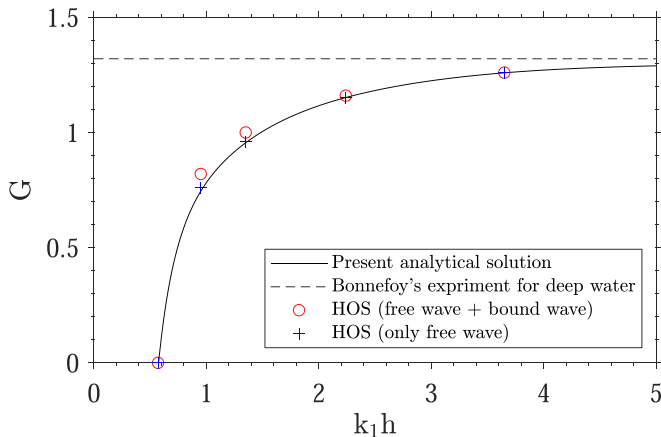


FIG. 13. Comparison of the growth rate obtained from HOS simulations and theoretical predictions using Eq. (19) for different water depths. The experimental data for deep water in Bonnefoy *et al.* [8] is also plotted for reference (dashed black line).

those from Eq. (19). However, with decreasing water depth, the effect of the bound waves becomes more noticeable. After removing bound waves, the tendency of the HOS results with respect to water depth is in better agreement with that based on Eq. (19). The bound wave effect is also confirmed by numerical simulations with using small mother-wave steepness (see Appendix C). Furthermore, as shown in the figure, it is confirmed that the four-wave resonance ceases to exist for $k_1 h \leq 0.57$, which agrees with the theoretical prediction presented in Fig. 2.

C. Quasiresonant four-wave interaction in finite depth

Here, we investigate the four-wave quasiresonant interactions of Set C. The wave numbers of the mother waves were selected to be the same as those in Set A. When the same wave number resonance condition is used in finite water depth, the resonance conditions cannot be satisfied anymore owing to the change in the dispersion relationship. However, quasiresonant nonlinear wave interactions can occur instead.

In Fig. 14, the free-surface elevation distribution and localized wave crest pattern of the quasiresonant wave system recorded at different times are presented for an intermediate water depth $k_1 h = 2.45$. We observed that the new crest generation phenomenon disappears, in contrast to the results of the case of exact resonant interaction. This is because the energy transfer between different scales induced by quasiresonant interaction is less pronounced, for example, the scale of the daughter-wave amplitude is relatively smaller than that in the case of resonant interactions. However, the quasiresonant interaction can still lead to a slightly enhanced formation of the localized crest shape. As shown in Fig. 14(e), the localized single crest becomes higher and steeper at $t/T_4 = 30$ and decreases to a minimum at $t/T_4 = 60$, as shown in Fig. 14(f). To examine the wave crest height, the wave height $\eta_{\max} - \eta_{\min}$ was plotted as a function of the propagation distance d , as illustrated in Fig. 15. This confirms the variation of the crest shape during the evolution of the nonlinear wave fields. In fact, we find that this can be attributed to the oscillatory evolution of the daughter-wave amplitude, as illustrated in Fig. 16. Figure 16 presents the HOS results of the daughter-wave amplitude and interaction phase as a function of the propagating distance d for different water depths. As can be observed, for $k_1 h = 2.45$, the first two maxima of the daughter-wave amplitude occur at approximately $d = 20$ m and 60 m, which is almost synchronous with the maximum crest heights observed in Fig. 15. From Eq. (17), one can show that the daughter-wave amplitude varies as a $|\sin|$ function with a period of $d = 2\pi c_{g4}/\Delta\Omega$. The interaction phase varies periodically between $-\pi/2$ and $\pi/2$ with the same period, referring to Eq. (18). For intermediate-depth cases

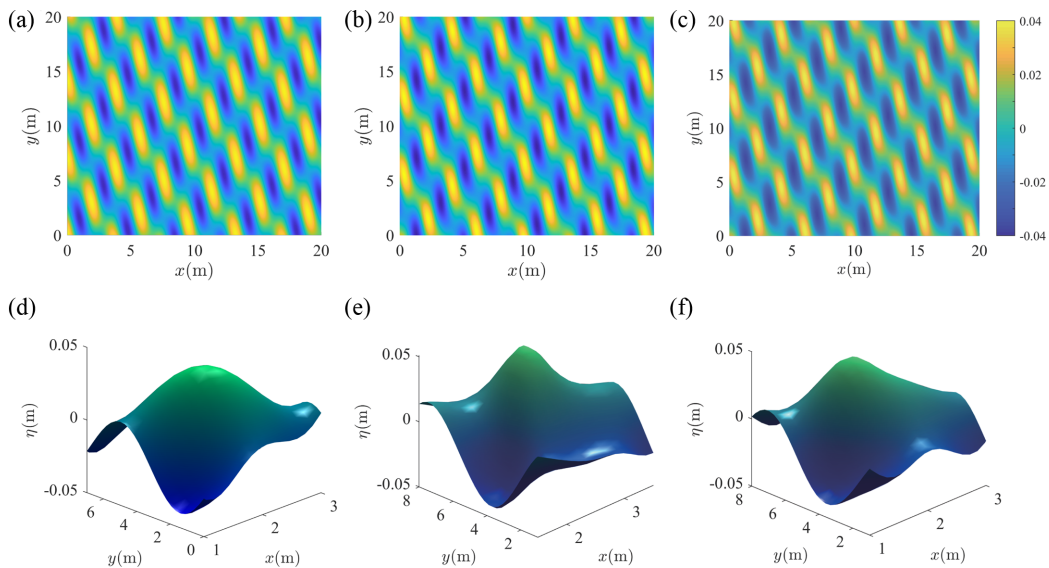


FIG. 14. Free-surface elevation (a–c) and corresponding localized crest shape (d–f) in finite-depth quasiresonant case (Set C, $k_1 h = 2.45$) recorded at different times: $t/T_4 = 0$ (a, d), 30 (b, e), and 60 (c, f).

$k_1 h = 3.65, 2.24, 1.35, 0.95$, as expected, the daughter-wave amplitude varies periodically as a $|\sin|$ function, and the interaction phase changes between $-\pi/2$ and $\pi/2$. Furthermore, the period of amplitude recurrence and variation of the phase between $-\pi/2$ and $\pi/2$ are the same. For example, with $k_1 h = 2.45$, the period of amplitude recurrence is approximately 37 m, and the period of phase change between $-\pi/2$ and $\pi/2$ is approximately the same. In the case of the shallowest water depth of $k_1 h = 0.49$, there was no clear tendency in the evolution, which is consistent with the vanished growth rate of the daughter wave.

To investigate the effect of bound waves, the space-time amplitude spectra of the quasiresonant systems were evaluated. Examples of $t = 50T_4$ are shown in Fig. 17. Similar to the exact-resonant cases, with decreasing water depth, more bound-wave peaks are observed and the bound wave at $|2\mathbf{k}_1 - \mathbf{k}_3|$ increased as the depth becomes shallow enough (that is, $k_1 h = 0.98$ and 0.49). Further-

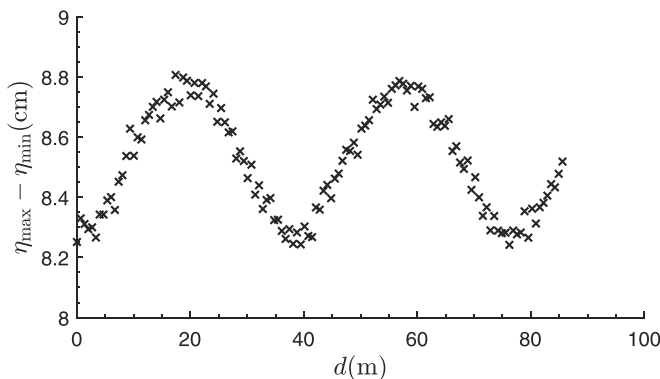


FIG. 15. Variation of $\eta_{\max} - \eta_{\min}$ with respect to d obtained from HOS simulations for the resonant case of finite water depth $k_1 h = 2.45$ of Set C. Here, η_{\max} and η_{\min} are the maximum value and minimum value of the free-surface elevations, respectively.

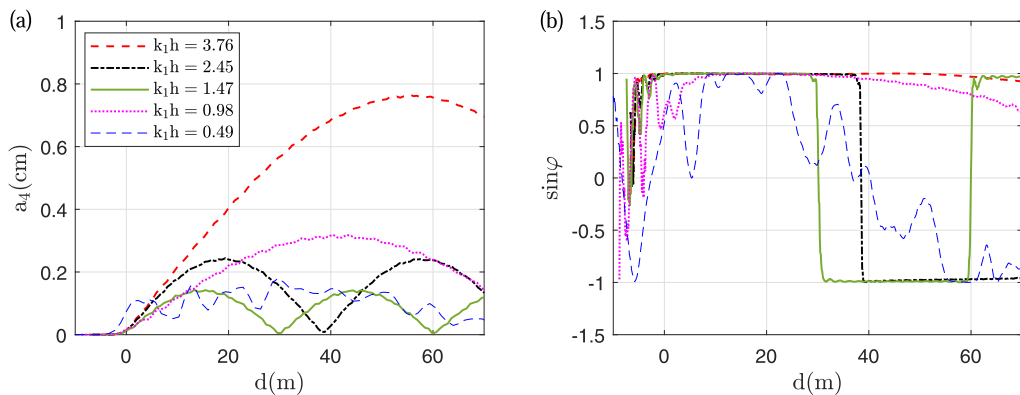


FIG. 16. Evolution of finite-depth quaresonant waves (Set C): (a) daughter-wave amplitude, (b) the sine of interaction phase.

more, we can observe more energy concentrates around the linear dispersion curve, which suggests higher harmonics are generated owing to wave-wave interaction as the water depth decreases. These results can complement our understanding from the analytical solution, which only considers three waves.

To examine the development of the daughter wave without bound wave effect, the space-time spectra for the two shallow-water cases ($k_1h = 0.98$ and 0.49) are evaluated for every five periods. The evolution of the free-wave amplitude and phase at $|2\mathbf{k}_1 - \mathbf{k}_3|$ was then obtained, as shown in Fig. 18, and compared with the results that include both free and bound waves. As can be observed in the figure, for $k_1h = 0.98$, the daughter-wave amplitude first increases and then decreases to zero,

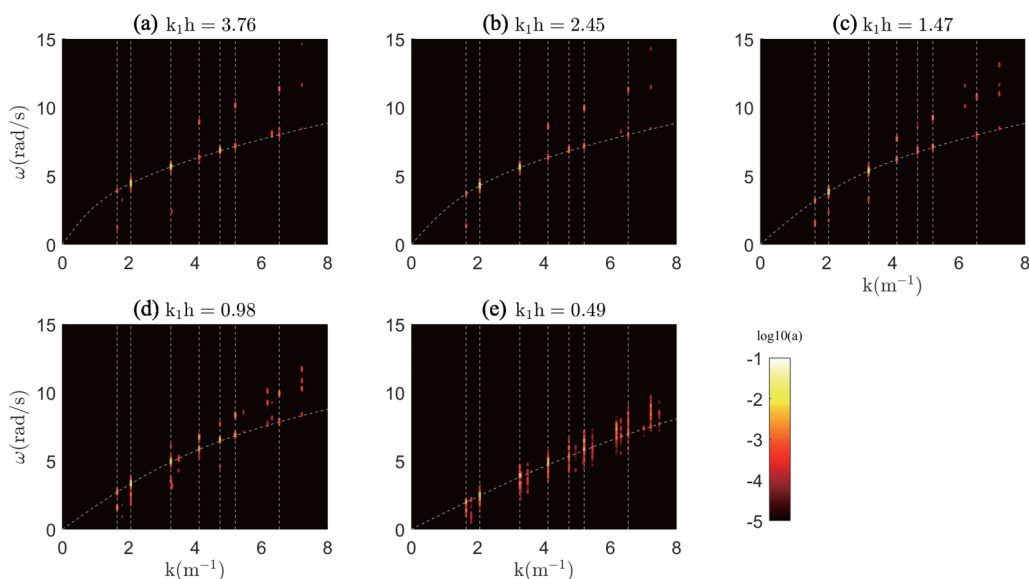


FIG. 17. Space-time in finite-depth quaresonant cases (Set C). The solid line represents the linear dispersion relation. Vertical dotted lines denote the wave numbers in the order of: $|\mathbf{k}_1 - \mathbf{k}_3|$, $|\mathbf{k}_3|$, $|\mathbf{k}_1|$, $|2\mathbf{k}_3|$, $|2\mathbf{k}_1 - \mathbf{k}_3|$, $|\mathbf{k}_1 + \mathbf{k}_3|$, and $|2\mathbf{k}_1|$.

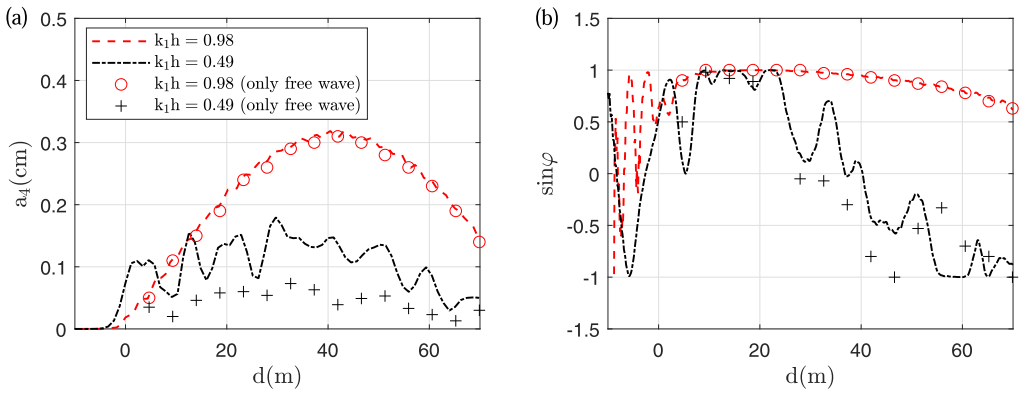


FIG. 18. Effect of bound waves on the evolution of daughter-wave in quasiresonant interactions: (a) wave amplitude, (b) interaction phase.

while the interaction phases remain around $\pi/2$. This can be explained by Eq. (16), which shows that the phase angle depends on the sign of $\sin(\Delta\Omega t/2)$.

In addition, as can be observed in Fig. 18 for $k_1 h = 0.98$, with the bound waves being included, the daughter-wave amplitude slightly increases during the early time and the interaction phase also varies slightly. However, for $k_1 h = 0.49$, the bound wave effect was significantly enhanced, particularly shown in the evolution of the interaction phase. In addition, even without a bound wave, the daughter-wave amplitude initially increases rapidly. It can be inferred that other higher-harmonic free waves are generated and interact with the mother waves.

Figure 19 compares the theoretical results from Eq. (17) with the HOS results for resonant interactions in Set B and quasiresonant interaction in Set C. For reference, we also present the experimental data for deep-water waves in Bonnefoy *et al.* [8]. Note that the HOS results presented here only include free wave effects. Comparing with the HOS results for resonant interactions and quasiresonant interaction, it was observed that they share a consistent tendency of the growth rate with respect to water depth $k_1 h$. Furthermore, results for resonant interaction using the HOS method

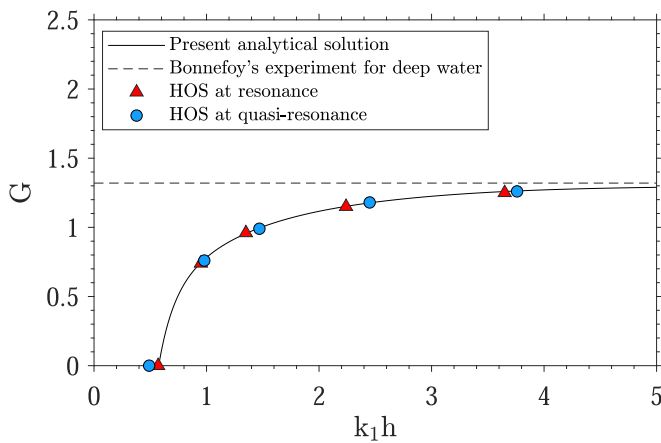


FIG. 19. Growth rate of daughter-wave amplitude as a function of nondimensional water depth $k_1 h$ with crossing angle $\theta = 25^\circ$. It includes the results from quasiresonant simulations and resonant simulations, as well as those from Eq. (17). The experimental data for deep water in Bonnefoy *et al.* [8] is also plotted for reference (dashed black line).

and Eq. (19) show a similar tendency that the growth rate is gradually suppressed with the decreasing water depth and eventually approaches zero at a sufficiently shallow depth. It should be noted that the solutions from the theoretical model based on the Zakharov equation are only valid for a small distance d when the amplitude of the daughter wave has not grown sufficiently to be comparable to the mother-wave amplitude, which is the assumption used to derive Eqs. (14) and (16).

V. CONCLUDING REMARKS

In the present study, four-wave resonant and quasis resonant nonlinear interactions at different water depths were investigated using analytical formulas derived from Zakharov equation and direct numerical simulations using the HOS. Herein, we focused on the degenerated case, where bichromatic mother waves are generated initially to give birth to a daughter wave. We analyzed the evolution of the daughter-wave amplitude and phase with respect to the mother waves, as well as the wave shape in the field.

The present theoretical solutions based on the Zakharov equation only considers the interaction of the free waves. However, in the HOS simulations, both the free and bound waves were included so that the interaction between different harmonics is consisted. To examine the bound-wave effect, space-time spectrum analyses were performed using the three-dimensional Fourier transform technique. The present results imply that the effect of the bound wave is not significant in deep water. However, with the decreasing water depth, the bound wave effect becomes more pronounced, particularly in the resonant cases of $k_1 h = 0.95, 0.57$, and quasis resonant cases of $k_1 h = 0.98, 0.49$. To examine the bound wave effect, the evolution of daughter waves in these cases was reproduced based on the space-time spectra using the 3D-FFT technique.

For the first time, with the support of analytical and numerical results, we found that four-wave resonant and quasis resonant interactions are suppressed as the water depth decreases and eventually diminish in sufficiently shallow waters. Four-wave resonance and quasis resonance between mother waves with a crossing angle of $\theta = 25^\circ$ cease to exist when the nondimensional depth approaches $k_1 h \leq 0.57$. Moreover, theoretical analyses suggest that the critical depth depends on the crossing angle, and almost all the four-wave resonant interactions with different crossing angles cease to exist for values of $k_1 h$ that are less than a global threshold value of approximately 0.4.

In the shallow-water condition, higher harmonics, owing to nonlinear wave-wave interaction, were observed, in particular as the mother-wave steepness increases. In addition, we found that the bound wave effect is enhanced as the water depth decreases, in particular when the mother-wave steepness increases.

It is worth noting that a flat-bottom boundary condition is assumed in the present study. As the effect of bottom topography is included, the four-wave interaction becomes more complicated and can play a significant role in the generation of oceanic extreme waves and the evolution of the spectrum [39–41]. Further investigation on the effects of bottom topography on the four-wave resonance is needed to better understand the statistical properties of extreme waves.

ACKNOWLEDGMENTS

The financial support from the National Natural Science Foundation of China through Grant No. 52171269 is gratefully acknowledged. X.Z. and S.L. are very grateful for the financial support from the Oceanic Interdisciplinary Program of Shanghai Jiao Tong University (Project No. SL2021PT205). The assistance from J. Yao for preparing this paper is appreciated.

APPENDIX A: EXPRESSION OF THE KERNEL T_{1212}

Herein, we show the expression of the interaction kernel T_{1212} from Stiassnie and Gramstad [29]. The kernel can be decomposed into regular and singular parts,

$$T_{1212} \equiv T(\mathbf{k}_1, \mathbf{k}_2, \mathbf{k}_1, \mathbf{k}_2) = T_{1212}^{(R)} + T_{1212}^{(S)}. \quad (\text{A1})$$

The regular part $T_{1212}^{(R)}$ can be written as

$$\begin{aligned}
 T_{1212}^{(R)} = & \frac{g}{32\pi^2\omega_1\omega_2} \left(-2\frac{\omega_1^2\omega_2^2}{g^2}(k_1^2 + k_2^2) \right. \\
 & + \frac{1}{\omega_{1-2}^2 - (\omega_1 - \omega_2)^2} \left\{ [\omega_2(k_1^2 - \mathbf{k}_1 \cdot \mathbf{k}_2) - \omega_1(k_2^2 - \mathbf{k}_1 \cdot \mathbf{k}_2)] \right. \\
 & \times \left[-\omega_2(k_1^2 - 3\mathbf{k}_1 \cdot \mathbf{k}_2) + \omega_1(k_2^2 - 3\mathbf{k}_1 \cdot \mathbf{k}_2) + 2\frac{\omega_1^2\omega_2^2}{g^2}(\omega_1 - \omega_2) \right] \\
 & - \left[(\mathbf{k}_1 \cdot \mathbf{k}_2)^2 + 2\frac{\omega_1\omega_2^3}{g^2}(k_1^2 - 2\mathbf{k}_1 \cdot \mathbf{k}_2) - 2\frac{\omega_1^2\omega_2^2}{g^2}(k_1^2 + k_2^2 - 3\mathbf{k}_1 \cdot \mathbf{k}_2) \right. \\
 & \left. \left. + 2\frac{\omega_1^3\omega_2}{g^2}(k_2^2 - 2\mathbf{k}_1 \cdot \mathbf{k}_2) + \frac{\omega_1^2\omega_2^2}{g^4}(\omega_1^2 - \omega_1\omega_2 + \omega_2^2)^2 \right] \omega_{1-2}^2 \right\} \\
 & - \frac{1}{\omega_{1+2}^2 - (\omega_1 + \omega_2)^2} \left\{ [\omega_2(k_1^2 + \mathbf{k}_1 \cdot \mathbf{k}_2) + \omega_1(k_2^2 + \mathbf{k}_1 \cdot \mathbf{k}_2)] \right. \\
 & \times \left[\omega_2(k_1^2 + 3\mathbf{k}_1 \cdot \mathbf{k}_2) + \omega_1(k_2^2 + 3\mathbf{k}_1 \cdot \mathbf{k}_2) + 2\frac{\omega_1^2\omega_2^2}{g^2}(\omega_1 + \omega_2) \right] \\
 & + \left[(\mathbf{k}_1 \cdot \mathbf{k}_2)^2 - 2\frac{\omega_1\omega_2^3}{g^2}(k_1^2 + 2\mathbf{k}_1 \cdot \mathbf{k}_2) - 2\frac{\omega_1^2\omega_2^2}{g^2}(k_1^2 + k_2^2 + 3\mathbf{k}_1 \cdot \mathbf{k}_2) \right. \\
 & \left. \left. - 2\frac{\omega_1^3\omega_2}{g^2}(k_2^2 + 2\mathbf{k}_1 \cdot \mathbf{k}_2) + \frac{\omega_1^2\omega_2^2}{g^4}(\omega_1^2 + \omega_1\omega_2 + \omega_2^2)^2 \right] \omega_{1+2}^2 \right\} \Bigg). \tag{A2}
 \end{aligned}$$

The singular part $T_{1212}^{(S)}$ can be written as

$$\begin{aligned}
 T_{1,2,1,2}^{(S)} = & -\frac{g}{16\pi^2(gh - Cg_2^2)} \left\{ \left(k_1^2 - \frac{\omega_1^4}{g^2} \right) \left(k_2^2 - \frac{\omega_2^4}{g^2} \right) \frac{gh}{2\omega_1\omega_2} \right. \\
 & \left. + k_1k_2 \left[2 + \frac{Cg_2}{k_2\omega_2} \left(k_2^2 - \frac{\omega_2^4}{g^2} \right) \right] \cos\theta + \frac{Cg_2k_2}{\omega_1} \left(k_1^2 - \frac{\omega_1^4}{g^2} \right) \right\}, \tag{A3}
 \end{aligned}$$

where Cg represents the group velocity.

APPENDIX B: DERIVATION OF THE ANALYTICAL SOLUTION OF THE EVOLUTION EQUATIONS

Herein, we show the derivation of Eqs. (11), (12), and (13). By expanding all the functions as power series in ε , and collecting the leading-order terms at $\mathcal{O}(\varepsilon^0)$, it yields

$$i\partial_t B_4^0 = (\Omega_4 - \omega_4)B_4^0 + 2T_{1134} \exp(i\Delta_{1134}t) (B_1^0)^2 B_3^0, \tag{B1}$$

By solving the aforementioned equation with the initial condition $B_4^0|_{t=0} = 0$ (see the Supplemental Material of Bonnefoy *et al.* [8] for details), the solution can be recovered as

$$B_4^0 = -iT_{1134}B_{10}^2 B_{30}^* \frac{\sin(\Delta\Omega t/2)}{\Delta\Omega/2} \exp[-i(\Omega_4 - \omega_4 + \Delta\Omega/2)t]. \tag{B2}$$

In addition, the evolution of daughter wave 4 can be written as the sum of the leading-order term and the extra higher-order terms (H.O.T),

$$B_4 = -iT_{1134}B_{10}^2 B_{30}^* \frac{\sin(\Delta\Omega t/2)}{\Delta\Omega/2} \exp[-i(\Omega_4 - \omega_4 + \Delta\Omega/2)t] + \text{H.O.T.} \tag{B3}$$

The next step is to determine B_1 . Assuming the daughter-wave amplitude is much smaller than those of the mother waves, that is, $|B_4| \ll |B_1|, |B_3|$. By expanding all the functions as power series in ε , the amplitude B_1, B_3 , and B_4 can be written as

$$B_1 = B_1^0 + \varepsilon B_1^1 + \mathcal{O}(\varepsilon^2), \quad (\text{B4})$$

$$B_3 = B_3^0 + \varepsilon B_3^1 + \mathcal{O}(\varepsilon^2), \quad (\text{B5})$$

$$B_4 = \varepsilon B_4^0 + \varepsilon^2 B_4^1 + \mathcal{O}(\varepsilon^3), \quad (\text{B6})$$

where we consider the first two orders. By substituting Eqs. (B4), (B5), and (B6) into Eq. (5), it yields

$$\begin{aligned} i\partial_t(B_1^0 + \varepsilon B_1^1) &= (\Omega_1 - \omega_1)(B_1^0 + \varepsilon B_1^1) \\ + 2T_{1134} \exp(i\Delta_{1134}t)(B_1^{0*} + \varepsilon B_1^{1*})(B_3^0 + \varepsilon B_3^1)(\varepsilon B_4^0 + \varepsilon^2 B_4^1). \end{aligned} \quad (\text{B7})$$

By collecting the leading-order terms at $\mathcal{O}(\varepsilon^0)$, we obtain

$$i\partial_t B_1^0 = (\Omega_1 - \omega_1)B_1^0. \quad (\text{B8})$$

Thus, we obtain

$$B_1^0 = B_{10} \exp[-i(\Omega_1 - \omega_1)t], \quad (\text{B9})$$

where the subscript ‘‘0’’ denotes the initial value of mother-wave amplitude.

For the second-order terms at $\mathcal{O}(\varepsilon^1)$, it leads to

$$i\partial_t B_1^1 = (\Omega_1 - \omega_1)B_1^1 + 2T_{1134} \exp(i\Delta_{1134}t)B_1^{1*}B_3^0B_4^0, \quad (\text{B10})$$

which shows that the solution of B_1^1 depends on B_4^0 .

Similarly, by substituting Eqs. (B4), (B5), and (B6) into Eq. (6), and collecting the terms at $\mathcal{O}(\varepsilon^0)$ and $\mathcal{O}(\varepsilon^1)$, respectively, it yields

$$B_3^0 = B_{30} \exp[-i(\Omega_3 - \omega_3)t] \quad (\text{B11})$$

and

$$i\partial_t B_3^1 = (\Omega_3 - \omega_3)B_3^1 + 2T_{1134} \exp(i\Delta_{1134}t)B_1^0B_1^0B_4^{0*}, \quad (\text{B12})$$

which shows that the solution of B_3^1 depends on B_4^0 .

Substituting Eq. (B2) into Eq. (B12), we can show

$$B_1^1 = 2T_{1134}^2 B_{10}^2 B_{10}^* B_{30}^* B_{30} \left[\frac{1 - \exp(-i\Delta\Omega t)}{\Delta\Omega^2} - \frac{it}{\Delta\Omega} \right] \exp[i(\omega_1 - \Omega_1)t]. \quad (\text{B13})$$

Following the same procedures as for the mother wave 3, we obtain,

$$B_3^1 = T_{1134}^2 B_{10}^2 B_{10}^{*2} B_{30} \left[\frac{1 - \exp(i\Delta\Omega t)}{\Delta\Omega^2} - \frac{it}{\Delta\Omega} \right] \exp[i(\omega_3 - \Omega_3)t]. \quad (\text{B14})$$

Substituting Eqs. (B9) and (B13) into Eq. (B4), respectively, we obtain

$$B_1 = \left\{ B_{10} - 2T_{1134}^2 B_{10}^2 B_{10}^* B_{30}^* B_{30} \left[\frac{1 - \exp(-i\Delta\Omega t)}{\Delta\Omega^2} - \frac{it}{\Delta\Omega} \right] \right\} \exp[i(\omega_1 - \Omega_1)t]. \quad (\text{B15})$$

Substituting Eqs. (B11) and (B14) into Eq. (B5),

$$B_3 = \left\{ B_{30} + T_{1134}^2 B_{10}^2 B_{10}^{*2} B_{30} \left[\frac{1 - \exp(i\Delta\Omega t)}{\Delta\Omega^2} - \frac{it}{\Delta\Omega} \right] \right\} \exp[i(\omega_3 - \Omega_3)t]. \quad (\text{B16})$$

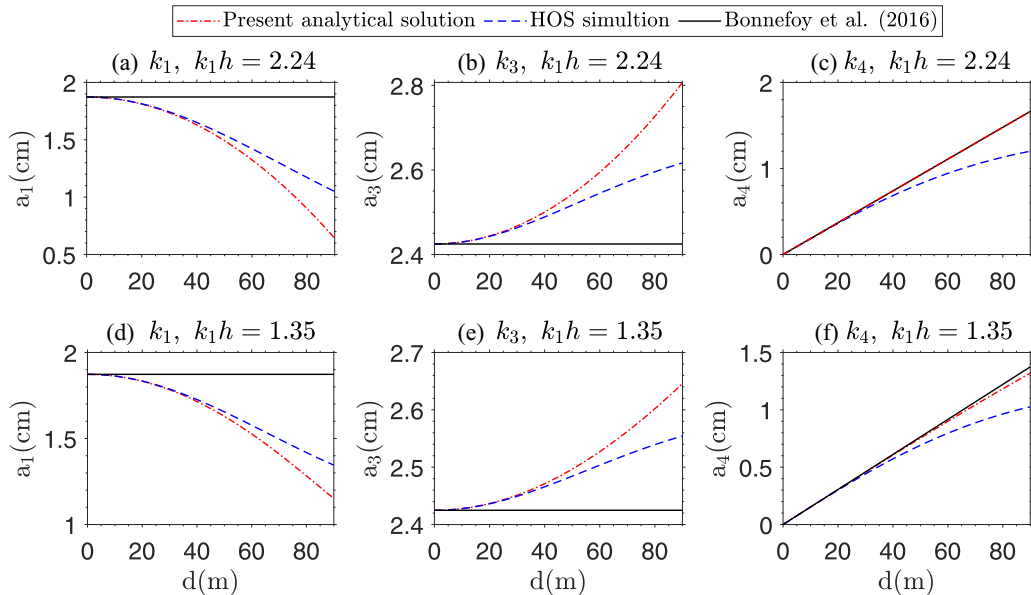


FIG. 20. The evolution of wave amplitude a_1 , a_3 and a_4 at $k_1h = 2.24, 1.35$ in Set B. The analytical solutions obtained from Eqs. (11), (12), and (13) are compared with those using HOS.

It should be noted that the relation between the free-surface wave amplitude and wave action amplitude B_i is $a_i = \sqrt{2\omega_i/gB_i}$. Figure 20 shows the comparison of the results using analytical formulas with the results using HOS. As can be observed, a good agreement is observed in the initial stage of the evolution.

APPENDIX C: DIRECT NUMERICAL SIMULATIONS USING SMALL MOTHER-WAVE STEEPNESS

In HOS simulation, both bound and free waves triggered by nonlinear wave interactions are considered. However, in the theoretical solutions based on the Zakharov equation only free-wave components are retained. For this reason, the growth rate of the daughter wave from the HOS simulation is slightly larger than that from the theoretical solutions of Eq. (19) at shallow depths, where the effect of bound waves is nonnegligible (referring to Fig. 13). Nevertheless, attributed to the windowed three-dimensional Fourier transform, the bound wave in HOS simulations can be also removed using the $k - \omega$ plot. As expected, if only the free wave effect is considered, the results of HOS are in good agreement with those from Eq. (19) (referring to Fig. 13).

To minimize the bound-wave effect, another approach is to reduce the mother-wave amplitudes (equivalent to a reduction in wave steepness). As ε_1 and ε_3 reduce, the amplitudes of their bound waves reduce, but the growth rate of the daughter wave is not varied [referring to Eq. (19)]. Thus, the effect of bound waves on the generation of the daughter wave is suppressed. Herein, the steepness decreases to $\varepsilon_1 = 0.0056$, $\varepsilon_3 = 0.0050$, while the other parameters are the same as those chosen in Set B.

The evolution of daughter-wave amplitude is shown in Fig. 21, where the results with steeper mother waves from Fig. 9 and the prediction of Eq. (14) are also plotted for comparisons. For the case of $k_1h = 1.35$, either large or small $\varepsilon_1, \varepsilon_3$, the results are in good agreement with the predictions of Eq. (14). In the case of $k_1h = 0.95$, where the influence of bound wave is more significant, HOS results with larger steepness show a difference from those using Eq. (14). However, as the ε_1 and ε_3

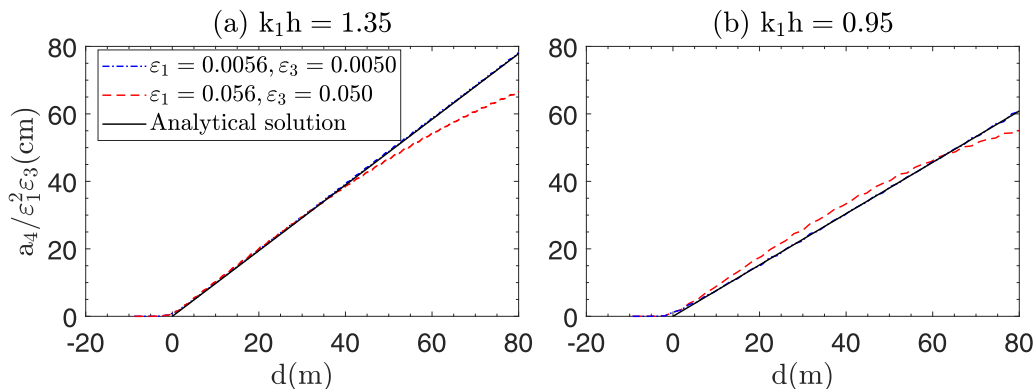


FIG. 21. The evolution of daughter-wave amplitude with larger and smaller wave steepness ϵ_1, ϵ_3 . The black solid line represents the analytical solution from Eq. (17).

are reduced, i.e., the bound wave effect is fully suppressed, so that the results of the HOS and the analytical solutions from discretized Zakharov equation are consistent.

-
- [1] K. Hasselmann, On the nonlinear energy transfer in a gravity-wave spectrum, *J. Fluid Mech.* **12**, 481 (1962).
 - [2] O. M. Phillips, On the dynamics of unsteady gravity waves of finite amplitude Part 1. The elementary interactions, *J. Fluid Mech.* **9**, 193 (1960).
 - [3] M. S. Longuet-Higgins, Resonant interactions between two trains of gravity waves, *J. Fluid Mech.* **12**, 321 (1962).
 - [4] M. S. Longuet-Higgins and N. D. Smith, An experiment on third-order resonant wave interactions, *J. Fluid Mech.* **25**, 417 (1966).
 - [5] M. F. McGoldrick, O. M. Phillips, N. E. Huang, and T. H. Hodgson, Measurements of third-order resonant wave interactions, *J. Fluid Mech.* **25**, 437 (1966).
 - [6] M. Tomita, Theoretical and experimental investigations of interaction among deep-water gravity waves, *Rep. Ship Res. Inst.* **26**, 251 (1989).
 - [7] M. Onorato, A. R. Osborne, P. A. E. M. Janssen, and D. Resio, Four-wave resonant interactions in the classical quadratic Boussinesq equations, *J. Fluid Mech.* **627**, 235 (2009).
 - [8] F. Bonnefoy, F. Haudin, G. Michel, B. Semin, T. Humbert, S. Aumaitre, M. Berhanu, and E. Falcon, Observation of resonant interactions among surface gravity waves, *J. Fluid Mech.* **805**, R3 (2016).
 - [9] V. E. Zakharov, Stability of periodic waves of finite amplitude on the surface of a deep fluid, *J. Appl. Mech. Tech. Phys.* **9**, 190 (1968).
 - [10] T. B. Benjamin, Instability of periodic wavetrains in nonlinear dispersive systems, *Proc. R. Soc. London* **299**, 59 (1967).
 - [11] G. B. Whitham, Linear and nonlinear waves, in *Pure and Applied Mathematics* (Wiley, New York, 1974).
 - [12] P. A. E. M. Janssen and M. Onorato, The intermediate water depth limit of the Zakharov equation and consequences for wave prediction, *J. Phys. Oceanogr.* **37**, 2389 (2007).
 - [13] D. J. Benney and G. J. Roskes, Wave Instabilities, *Stud. Appl. Math.* **48**, 377 (1969).
 - [14] C. Kharif and E. Pelinovsky, Physical mechanisms of the rogue wave phenomenon, *Eur. J. Mech. B Fluids* **22**, 603 (2003).
 - [15] A. Toffoli, L. Fernandez, J. Monbaliu, M. Benoit, E. Gagnaire-Renou, J. M. Lefvre, L. Cavaleri, P. Proment, D. C., and C. T. Stansberg, Experimental evidence of the modulation of a plane wave to oblique perturbations and generation of rogue waves in finite water depth, *Phys. Fluids* **25**, 091701 (2013).

- [16] L. Fernandez, M. Onorato, J. Monbaliu, and A. Toffoli, Modulational instability and wave amplification in finite water depth, *Nat. Haz. Earth Syst. Sci.* **14**, 705 (2014).
- [17] A. Toffoli, M. Benoit, M. Onorato, and E. M. Bitner-gregersen, The effect of third-order nonlinearity on statistical properties of random directional waves in finite depth, *Nonlin. Process. Geophys.* **16**, 131 (2009).
- [18] L. Fernandez, M. Onorato, J. Monbaliu, and A. Toffoli, Occurrence of extreme waves in finite water depth, in *Extreme Ocean Waves* (Springer, Berlin, 2016), pp. 45–62.
- [19] P. Madsen and D. Fuhrman, Third-order theory for bichromatic bi-directional water waves, *J. Fluid Mech.* **557**, 369 (2006).
- [20] J.-J. Xie, Y. Ma, G. Dong, and M. Perlin, Numerical investigation of third-order resonant interactions between two gravity wave trains in deep water, *Phys. Rev. Fluids* **6**, 014801 (2021).
- [21] D. Dommermuth and D. K. P. Yue, A higher-order spectral method for the study of nonlinear gravity waves, *J. Fluid Mech.* **184**, 267 (1987).
- [22] B. J. West, K. A. Brueckner, and R. S. Janda, A new numerical method for surface hydrodynamics, *J. Geophys. Res.* **92**, 11803 (1987).
- [23] A. Toffoli, O. Gramstad, K. Trulsen, J. Monbaliu, E. Bitner-Gregersen, and M. Onorato, Evolution of weakly nonlinear random directional waves: Laboratory experiments and numerical simulations, *J. Fluid Mech.* **664**, 313 (2010).
- [24] W. T. Xiao, Y. M. Liu, G. Y. Wu, and D. K. P. Yue, Rogue wave occurrence and dynamics by direct simulations of nonlinear wave-field evolution, *J. Fluid Mech.* **720**, 357 (2013).
- [25] O. Gramstad, E. M. Bitner-Gregersen, K. Trulsen, and J. Nieto-Borge, Modulational instability and rogue waves in crossing sea states, *J. Phys. Oceanogr.* **48**, 1317 (2018).
- [26] F. Fedele, J. Brennan, S. Ponce De León, J. Dudley, and F. Dias, Real-world ocean rogue waves explained without the modulational instability, *Sci. Rep.* **6**, 27715 (2016).
- [27] W. Fujimoto, T. Waseda, and A. Webb, Impact of the four-wave quasisresonance on freak wave shapes in the ocean, *Ocean Dyn.* **69**, 101 (2019).
- [28] V. Krasitskii, On reduced equations in the Hamiltonian theory of weakly nonlinear surface waves, *J. Fluid Mech.* **272**, 1 (1994).
- [29] M. Stiassnie and O. Gramstad, On Zakharov’s kernel and the interaction of noncollinear wave trains in finite water depth, *J. Fluid Mech.* **639**, 433 (2009).
- [30] T. Waseda, T. Kinoshita, L. Cavaleri, and A. Toffoli, Third-order resonant wave interactions under the influence of background current fields, *J. Fluid Mech.* **784**, 51 (2015).
- [31] M. Tanaka, A method of studying nonlinear random field of surface gravity waves by direct numerical simulations, *Fluid Dyn. Res.* **28**, 41 (2001).
- [32] M. Tanaka, Verification of Hasselmann energy transfer among surface gravity waves by direct numerical simulations of primitive equations, *J. Fluid Mech.* **444**, 199 (2001).
- [33] S. Liu and X. S. Zhang, Extreme wave crest distribution by direct numerical simulations of long-crested nonlinear wave fields, *Appl. Ocean Res.* **86**, 141 (2019).
- [34] D. Dommermuth, The initialization of nonlinear waves using an adjustment scheme, *Wave Motion* **32**, 307 (2000).
- [35] A. V. Slunyaev, Group-wave resonances in nonlinear dispersive media: The case of gravity water waves, *Phys. Rev. E* **97**, 010202(R) (2018).
- [36] D. Barratt, H. B. Bingham, P. H. Taylor, T. S. van den Bremer, and T. A. A. Adcock, *Directional energy transfer due to third-order interactions during an extreme wave event*, in *Proceedings of the 34th International Workshop on Water Waves and Floating Bodies, Newcastle, Australia, 2019* (IWWWFB, 2019).
- [37] A. Toffoli, M. Onorato, A. V. Babanin, E. M. Bitner-Gregersen, A. R. Osborne, and J. Monbaliu, Second-order theory and setup in surface gravity waves: A comparison with experimental data, *J. Phys. Oceanogr.* **37**, 2726 (2007).
- [38] J. Dalzell, A note on finite depth second-order wave–wave interactions, *Appl. Ocean Res.* **21**, 105 (1999).
- [39] M. Gouin, G. Ducrozet, and P. Ferrant, Development and validation of a nonlinear spectral model for water waves over variable depth, *Eur. J. Mech. B Fluids* **57**, 115 (2016).

- [40] J. Zhang and B. Michel, Wave–bottom interaction and extreme wave statistics due to shoaling and de-shoaling of irregular long-crested wave trains over steep seabed changes, *J. Fluid Mech.* **912**, A28 (2021).
- [41] Z. Lyu, N. Mori, and H. Kashima, Freak wave in high-order weakly nonlinear wave evolution with bottom topography change, *Coast. Eng.* **167**, 103918 (2021).